

PUBLISHER :



Address of Publisher
& Editor's Office :

GDAŃSK UNIVERSITY
OF TECHNOLOGY
Faculty
of Ocean Engineering
& Ship Technology

ul. Narutowicza 11/12
80-952 Gdańsk, POLAND
tel.: +48 58 347 17 93
fax : +48 58 341 47 12
e-mail : sekoce@pg.gda.pl

Account number :
BANK ZACHODNI WBK S.A.
I Oddział w Gdańsku
41 1090 1098 0000 0000 0901 5569

Editorial Staff :

Witold Kirkor Editor in Chief
e-mail : pmrs@op.pl

Przemysław Wierzchowski Scientific Editor
e-mail : e.wierzchowski@chello.pl

Maciej Pawłowski Editor for review matters
e-mail : mpawlow@pg.gda.pl

Tadeusz Borzęcki Editor for international relations
e-mail : tadbtor@pg.gda.pl

Cezary Spigarski Computer Design
e-mail : biuro@oficynamorska.pl

Domestic price :
single issue : 20 zł

Prices for abroad :
single issue :
- in Europe EURO 15
- overseas US\$ 20

ISSN 1233-2585



POLISH MARITIME RESEARCH

in internet

www.bg.pg.gda.pl/pmr.html

Index and abstracts
of the papers
1994 ÷ 2005



POLISH MARITIME RESEARCH

No 4(50) 2006 Vol 13

CONTENTS

NAVAL ARCHITECTURE

- 3 **JAN A. SZANTYR**
*Scale effects in cavitation experiments
with marine propeller models*

MARINE ENGINEERING

- 11 **JANUSZ KOLENDĄ**
Effective fatigue damage summation
- 15 **STANISŁAW POLANOWSKI**
*Processing methods of measured runs
of torque and angular speed
of combustion engine propulsion system*

OPERATION & ECONOMY

- 23 **TADEUSZ SZELANGIEWICZ,
KATARZYNA ŹELAZNY**
*Calculation of the mean long-term service speed
of transport ship. Part I - Resistance
of ship sailing on regular shipping route
in real weather conditions*

The papers published in this issue have been reviewed by :

Assoc. Prof. Z. Chłopek ; Assoc. Prof. M. Pawłowski
Assoc. Prof. M. Sperski ; Prof. J. Szantyr



Photo : C. Spigarski

Editorial

POLISH MARITIME RESEARCH is a scientific journal of worldwide circulation. The journal appears as a quarterly four times a year. The first issue of it was published in September 1994. Its main aim is to present original, innovative scientific ideas and Research & Development achievements in the field of :

Engineering, Computing & Technology, Mechanical Engineering,

which could find applications in the broad domain of maritime economy. Hence there are published papers which concern methods of the designing, manufacturing and operating processes of such technical objects and devices as : ships, port equipment, ocean engineering units, underwater vehicles and equipment as well as harbour facilities, with accounting for marine environment protection.

The Editors of POLISH MARITIME RESEARCH make also efforts to present problems dealing with education of engineers and scientific and teaching personnel. As a rule, the basic papers are supplemented by information on conferences , important scientific events as well as cooperation in carrying out international scientific research projects.

Scientific Board

Chairman : Prof. **JERZY GIRTLEK** - Gdańsk University of Technology, Poland

Vice-chairman : Prof. **ANTONI JANKOWSKI** - Institute of Aeronautics, Poland

Vice-chairman : Prof. **MIROSLAW L. WYSZYŃSKI** - University of Birmingham, United Kingdom

Dr **POUL ANDERSEN**
Technical University
of Denmark
Denmark

Prof. **STANISŁAW GUCMA**
Maritime University of Szczecin
Poland

Prof. **YASUHIKO OHTA**
Nagoya Institute of Technology
Japan

Dr **MEHMET ATILAR**
University of Newcastle
United Kingdom

Prof. **ANTONI ISKRA**
Poznań University
of Technology
Poland

Prof. **ANTONI K. OPPENHEIM**
University of California
Berkeley, CA
USA

Prof. **GÖRAN BARK**
Chalmers University
of Technology
Sweden

Prof. **JAN KICIŃSKI**
Institute of Fluid-Flow Machinery
of PASci
Poland

Prof. **KRZYSZTOF ROSOCHOWICZ**
Gdańsk University
of Technology
Poland

Prof. **SERGIEJ I. BARSUKOW**
Army Institute of Odessa
Ukraine

Prof. **ZYGMUNT KITOWSKI**
Naval University
Poland

Dr **YOSHIO SATO**
National Traffic Safety
and Environment Laboratory
Japan

Prof. **MUSTAFA BAYHAN**
Süleyman Demirel University
Turkey

Prof. **JAN KULCZYK**
Wrocław University of Technology
Poland

Prof. **KLAUS SCHIER**
University of Applied Sciences
Germany

Prof. **MAREK DZIDA**
Gdańsk University
of Technology
Poland

Prof. **NICOS LADOMMATOS**
University College London
United Kingdom

Prof. **FREDERICK STERN**
University of Iowa,
IA, USA

Prof. **ODD M. FALTINSEN**
Norwegian University
of Science and Technology
Norway

Prof. **JÓZEF LISOWSKI**
Gdynia Maritime University
Poland

Prof. **JÓZEF SZALA**
Bydgoszcz University
of Technology and Agriculture
Poland

Prof. **PATRICK V. FARRELL**
University of Wisconsin
Madison, WI
USA

Prof. **JERZY MATUSIAK**
Helsinki University
of Technology
Finland

Prof. **TADEUSZ SZELANGIEWICZ**
Technical University
of Szczecin
Poland

Prof. **WOLFGANG FRICKE**
Technical University
Hamburg-Harburg
Germany

Prof. **EUGEN NEGRUS**
University of Bucharest
Romania

Prof. **WITALIJ W. SZCZAGIN**
State Technical University
of Kaliningrad
Russia

Prof. **BORIS A. TIKHOMIROV**
State Marine University
of St. Petersburg
Russia

Prof. **DRACOS VASSALOS**
University of Glasgow
and Strathclyde
United Kingdom

Scale effects in cavitation experiments with marine propeller models

Jan A. Szantyr
Gdańsk University of Technology

ABSTRACT



The paper presents an overview of specific scale effects encountered in the cavitation experiments with marine propeller models. These scale effects result from unavoidable dissimilarity between model and full scale flow phenomena. They may influence first of all inception of different forms of cavitation, but they also are visible in development and desinence of cavitation on propeller blades. These scale effects may be divided into five main categories, which are described in detail. The influence of these five categories of scale effects on the different aspects of cavitation performance of marine propellers is discussed.

Keywords: cavitation, marine propellers, model experiments, scale effect

INTRODUCTION

Model experiments with marine propellers are still an important element of the process of marine propeller design. A meaningful proportion of these experiments are devoted to cavitation phenomena themselves and to different consequences of cavitation. Marine propellers exhibit a variety of specific forms of cavitation, shown schematically in Fig.1. The main forms include sheet, bubble, vortex and cloud cavitation. All forms of cavitation are as a rule unsteady and during propeller blades motion they undergo a process of inception, development and desinence, either related to the unsteadiness of flow around the propeller or resulting from the inherent unsteadiness of the cavitation phenomena themselves. They may lead to many negative consequences, such as pulsating pressure field, hydro-acoustic signals, erosion etc. It is important that predictions of full scale cavitation behaviour of a propeller, made on the basis of model experiments, are realistic and accurate. This requires detailed knowledge of specific scale effects related to cavitation phenomena.

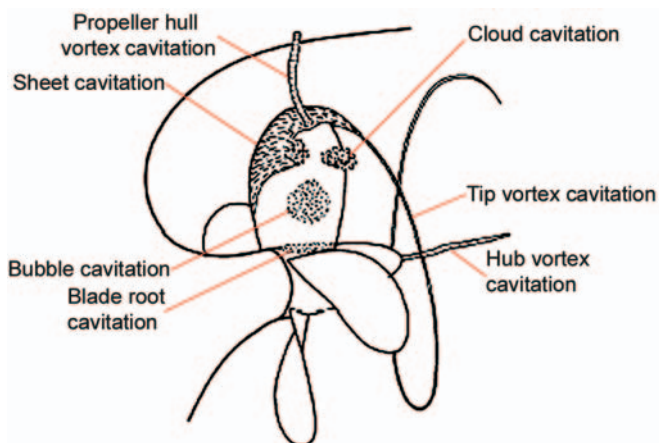


Fig. 1. Different forms of cavitation encountered on marine propellers.

With an exception of a few depressurized model basins, majority of model experiments with marine propellers are conducted in cavitation tunnels. As a rule these experiments are based on fulfilling two simple similarity criteria. The first criterion requires equality of model and full scale advance coefficients:

$$J_S = \frac{V_S}{n_S D_S} = J_M = \frac{V_M}{n_M D_M} \quad (1)$$

where :

- V – propeller advance velocity
- n – propeller number of revolutions
- D – propeller diameter
- index S – full scale (ship) values
- index M – model values.

This criterion ensures similarity of the basic kinematics of model and full scale flow around the propeller blades. However, this does not imply full similarity of flow in model and full scale, because Reynolds numbers in these two situations are markedly different. This leads to formation of different boundary layers in model and full scale. As a routine in the course of experiments it is only ensured that flow on the blades of a propeller model is supercritical, selecting sufficiently high number of propeller model revolutions to fulfil the following condition :

$$Re_M = \frac{0.75 \pi n_M D_M c_M}{v_M} \geq 5 \cdot 10^5 \quad (2)$$

where :

- c – blade section chord length at non-dimensional radius 0.75
- v – kinematic viscosity coefficient of water.

Full scale propeller Reynolds numbers are in the range $Re_s = 10^7$. In practice condition (2) does not always ensure fully

turbulent flow in model scale and regions of laminar flow may still be present on model propeller blades, especially near the hub. In full scale the flow is always turbulent from the leading edge. Other consequences of difference in model and full scale Reynolds numbers demonstrate themselves as differences in boundary layer separation or laminar/turbulent transition. These differences lead to the difference in open water characteristics, which require corrections [5] and they also have an influence on cavitation behaviour of the model and full scale propellers.

The second criterion requires equality of model and full scale cavitation number :

$$\sigma_S = \frac{p_A + \rho_S g h_s - p_{VS}}{\frac{1}{2} \rho_S V_{RS}^2} = \sigma_M = \frac{p_{TUN} - p_{VM}}{\frac{1}{2} \rho_M V_{RM}^2} \quad (3)$$

where :

- p_A – atmospheric pressure in full scale
- ρ – water density
- g – acceleration of gravity
- h – immersion of the point where cavitation number is defined
- p_V – critical pressure of water
- p_{TUN} – tunnel pressure at the point where cavitation number is defined
- V_R – reference velocity, either equal V or equal nD

The second criterion is expected to ensure the similarity of inception, growth and desinence of different cavitation phenomena present on marine propeller blades. However, it is known for many years now that cavitation phenomena are far too complex to be scaled properly by a single simple parameter like the cavitation number. Fulfilling relation (3) leaves a number of important scale effects due to the following reasons :

- ★ difference in static pressure distribution between the model and full scale propeller
- ★ difference in water quality – first of all in nuclei content
- ★ difference in boundary layer phenomena
- ★ difference in time and velocity scales
- ★ difference in size between model and full scale propeller.

These effects and their consequences are discussed in detail in the following sections. It is demonstrated that these scale effects may seriously affect the accuracy of full scale prediction of marine propeller cavitation performance made on the basis of model experiments.

THE EFFECT OF THE STATIC PRESSURE DISTRIBUTION

The typical scale coefficients of marine propeller models are in the range $\lambda = 20 - 30$. Let us consider for example a typical medium size propeller having the diameter $D_s = 6.0$ [m] and its shaft centre submerged at 9.0 [m] below free surface. Its model may have the diameter $D_M = 0.25$ [m]. It is obvious that criterion (3) may be fulfilled exactly only at one selected depth. Usually either shaft centre or blade tip in upper position are selected for this purpose. This situation is explained in Fig.2, where an exemplary distributions of model and full scale cavitation numbers along propeller blades are calculated assuming $\sigma_S = \sigma_M$ at blade tip.

As may be seen in Fig.2 there are quite meaningful differences in the distribution of cavitation numbers along the blades in vertical position, resulting from the different static pressure distribution in model and full scale. These differences may result in discrepancies between model and full scale cavitation

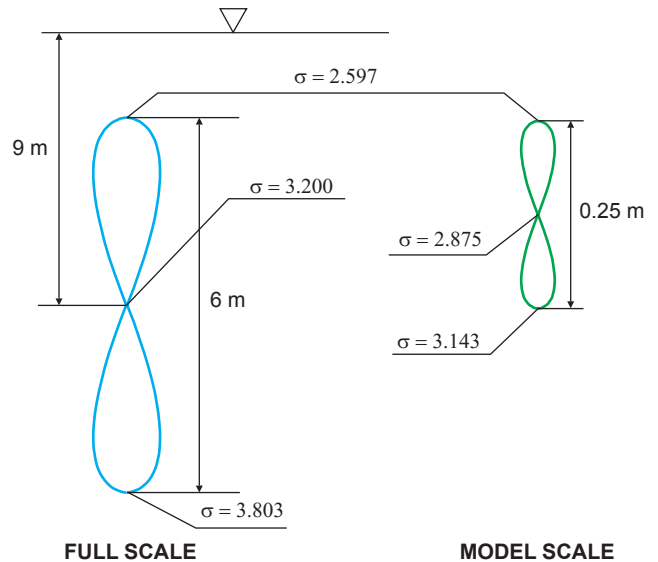


Fig. 2. Distribution of cavitation numbers along the blades of full scale and model propellers .

pictures on the blades in vertical positions and also in the time history of unsteady cavitation associated with blade motion in the non-uniform ship wake velocity field. In order to provide an assessment of importance of this effect Fig.3 shows two

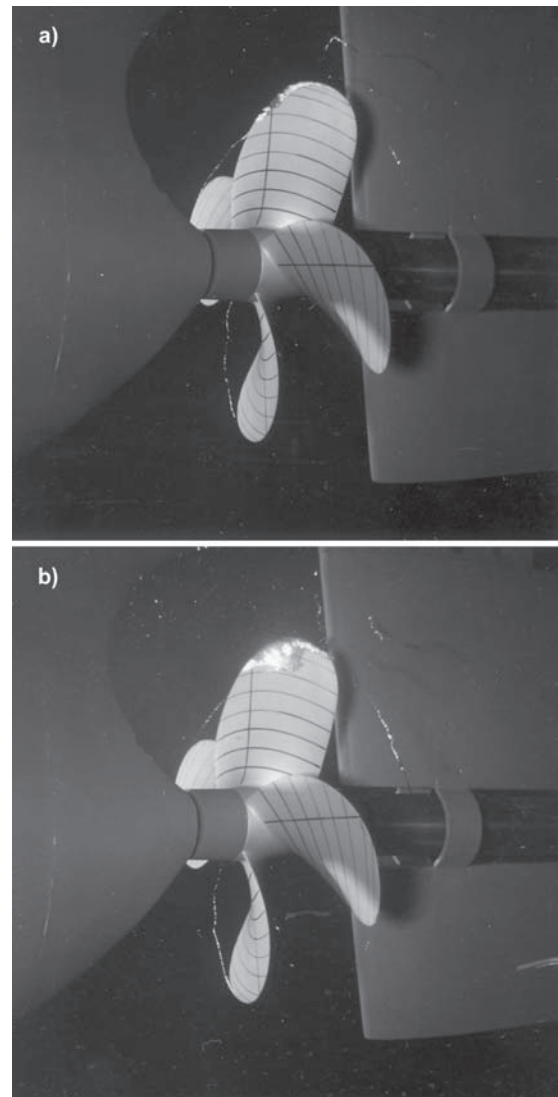


Fig. 3. Comparison of cavitation extent observed at : a) $\sigma_M = \sigma_S$ (blade tip) and b) $\sigma_M = \sigma_S$ (shaft centre).

photographs of cavitation extent on a model propeller blade in two conditions, namely with criterion (3) fulfilled at blade tip and at shaft centre. As may be seen in this figure, the difference is quite substantial. The expected full scale cavitation extent at blade top position should be somewhere in between the two pictures shown in Fig.3. Of course as in most cases cavitation phenomena are concentrated near the blade tip, the picture in Fig.3a may be regarded as closer to full scale reality. However, if the sheet cavity extends along most of the blade leading edge or we are specifically interested in the hub vortex formation, these effects may be decisive in proper scaling of the results.

The influence of static pressure distribution on the unsteady cavitation associated with blade rotation may be elucidated by comparing the variation of blade tip cavitation number with blade rotation in model and full scale, as shown in Fig.4. It may be seen in this figure that the rate of change of the cavitation number with blade position angle is much higher in full scale than in model scale. This may lead to a smaller angular extent of the cavitation phenomena on the blade in full scale than in model scale.

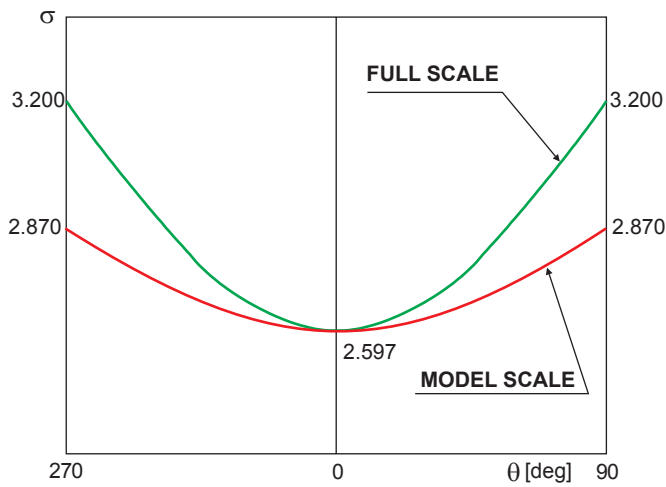


Fig. 4. Variation of the tip cavitation number with blade position angle .

In order to demonstrate the importance of this effect, cavitation sketches for different blade positions taken at different, appropriately chosen cavitation numbers are shown in Fig.5. In this figure three blade positions are shown, namely 315 [deg], i.e. 45 [deg] before reaching top, 0 [deg] and 45 [deg] after passing top. The upper row shows sketches at cavitation numbers corresponding to full scale at the respective blade positions, while the lower row shows sketches corresponding to model experiment with condition (3) fulfilled at blade tip in top position. These sketches should be of course treated only as a quasi-steady approximation of the real processes, but still it gives some idea about possible differences in scaling to full scale.

The scale effect discussed in this section may also influence other important cavitation characteristics of marine propellers, for example the propeller induced pressure pulsations, which are routinely measured in the cavitation tunnel and scaled for full scale. In this case setting condition (3) either at the blade tip or at the shaft centre leads to markedly different results which are shown in Tab.1. This table includes the amplitudes of the first three harmonics of pressure pulsations, given in [kPa] and starting with blade frequency. The pressure pulsations were measured in the cavitation tunnel and re-calculated into full scale values. The measurements refer to the point located immediately above propeller in the ship plane of symmetry. It may be seen that the alternative choice of setting condition (3) at blade tip or shaft centre produces almost 80 per cent difference, what correlates well with the pictures of cavitation in Fig.3. The true full scale prediction should be placed somewhere in between the two sets of values given in Tab.1, perhaps closer to the data for “blade tip” criterion.

Tab. 1. Pressure pulsations amplitudes in [kPa]

Harmonic no.	$\sigma_M = \sigma_s$ blade tip	$\sigma_M = \sigma_s$ shaft centre
1	405	235
2	155	94
3	122	67

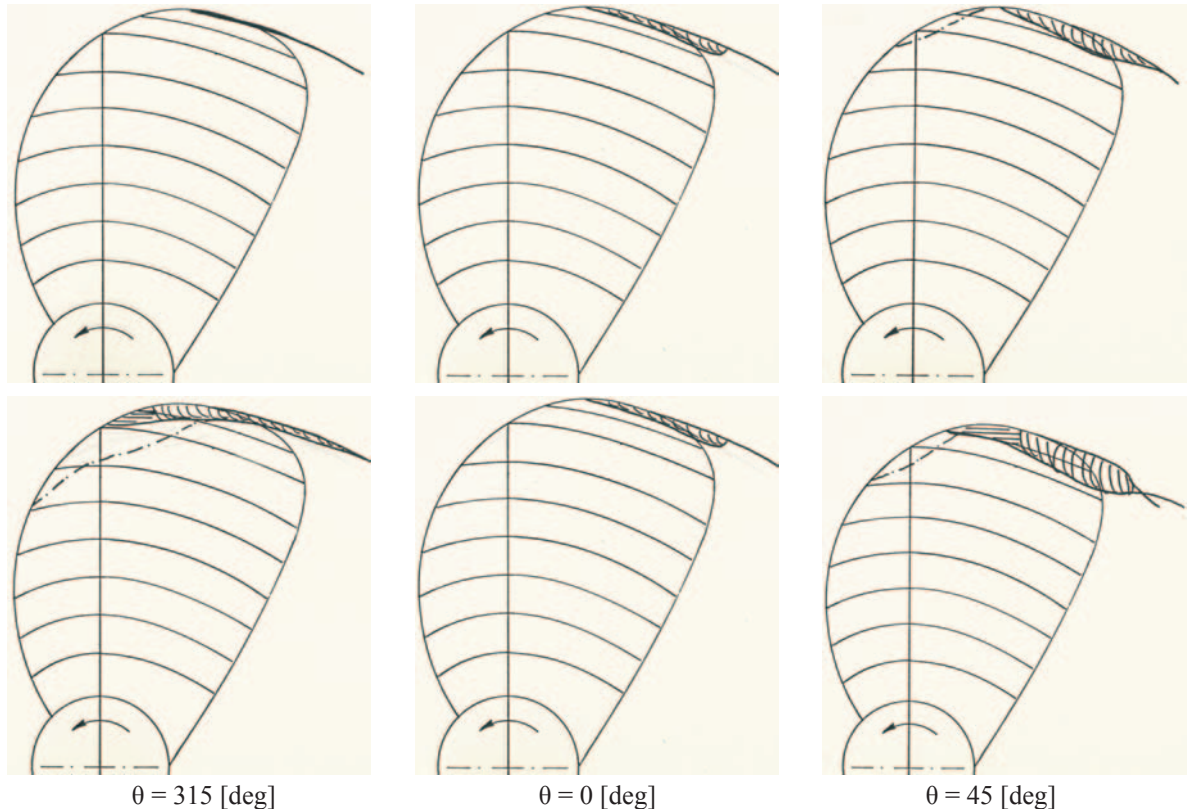


Fig. 5. Variation of sheet cavity with angular blade position observed in model scale (lower row) and simulated for full scale (upper row) .

THE EFFECT OF THE WATER QUALITY – NUCLEI CONTENT

From the point of view of cavitation the water quality in the experimental installation or at sea is described primarily by the dissolved air content, nuclei content and its previous history. In general there are meaningful differences in these parameters between the laboratory and full scale situations, which are the source of specific scale effects. These effects affect first of all the inception of cavitation, but they also have some influence on further development and desinence of cavitation. The detailed mechanisms of these scale effects are described below.

The classical cavitation similarity criterion (3) is based on the assumption that the critical pressure p_{CR} , i.e. pressure at which the liquid starts to rupture under tension and cavitation develops, is equal to the vapour pressure of the liquid p_v . However, it is known for quite a long time that the amount of tension that a liquid may withstand is substantial and it depends first of all on the dissolved gas content, nuclei content and previous history of the liquid. All these three factors are strongly inter-related with each other. Consequently, p_{CR} in most practical situations is not equal p_v and the cavitation number for inception of cavitation should be written in the following form :

$$\sigma_I = \frac{P_{TUN} - p_{CR}}{\frac{1}{2}\rho V_R^2} = \frac{P_{TUN} - (p_v - p_T)}{\frac{1}{2}\rho V_R^2} = \sigma + \frac{p_T}{\frac{1}{2}\rho V_R^2} = \sigma + \Delta\sigma \quad (4)$$

where :

- p_T – tensile strength of the liquid
 σ_I – inception cavitation number.

Then the cavitation inception condition should take the following form :

$$-C_{pmin} = \sigma_I \quad (5)$$

where : C_{pmin} is the non-dimensional minimum pressure coefficient on the tested object.

It would be very convenient if the value of p_T could be related directly to the nuclei content of the water. However, due to the complicated physics of cavitation inception this is not possible. Some guidance concerning this relation may be obtained from a simple condition for the stability of a single spherical vapour bubble, which is developed from the well-known Rayleigh Plesset equation [1] :

$$p_T = \frac{4S}{3R} \quad (6)$$

where :

- S – surface tension of water
 R – bubble radius.

Equation (6) shows that smaller bubbles can withstand higher tension and vice versa. In case of a random distribution of real nuclei the value of p_T may be either negative or positive, or in particular cases equal to zero. The liquid containing large bubbles exhibits negative tension strength in the sense that bubbles may grow due to diffusion without applying any tension to the liquid at all. On the contrary, liquid containing only a few small nuclei exhibits quite high positive tension strength. The dramatic effect of p_T on the cavitation phenomena

may be seen in Fig.6, showing cavitation phenomena on a wing at high positive p_T , at $p_T = 0$ and at negative p_T .

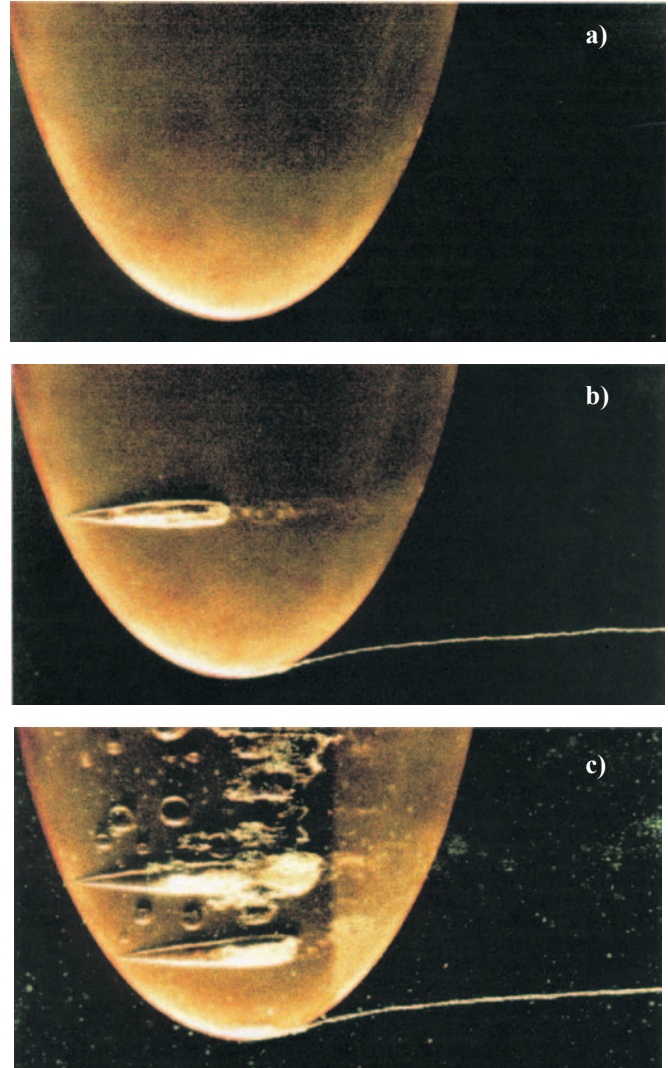


Fig. 6. Cavitation phenomena on a wing at high p_T (a), at $p_T = 0$ (b) and at negative p_T (c), quoted from [3].

As the value of p_T depends strongly on the nuclei content of the water and also on the dissolved air content, these two parameters should be controlled during experiments in the cavitation tunnel in such a way that consistent results are obtained and reliable scaling of the results into full scale is possible. Nuclei content in tunnel water may vary considerably, what is shown in Fig.7 taken from [1].

The influence of the nuclei distribution in water is visible first of all in determining the inception conditions for different forms of cavitation. This effect is illustrated in Fig.8, showing the variation in the cavitation inception number σ_I with nuclei concentration for three forms of cavitation: tip vortex cavitation, sheet cavitation and bubble cavitation. The effects shown in this figure may be explained in the following way :

- bubble cavitation is generated by rather small tension distributed widely over the central part of the propeller blade. This tension is able to destabilize only relatively large and sparsely distributed nuclei, hence its strong dependence on nuclei concentration
- sheet (surface) cavitation is generated by strong tension located in a narrow zone near the blade leading edge. This tension destabilizes even the smallest nuclei, hence its dependence on nuclei concentration is much weaker

tip vortex cavitation is initiated in a small volume around the centre of the vortex. Its inception depends on the probability of nuclei of suitable size flowing into that volume. This probability is the direct function of nuclei concentration, hence the dependence is strong.

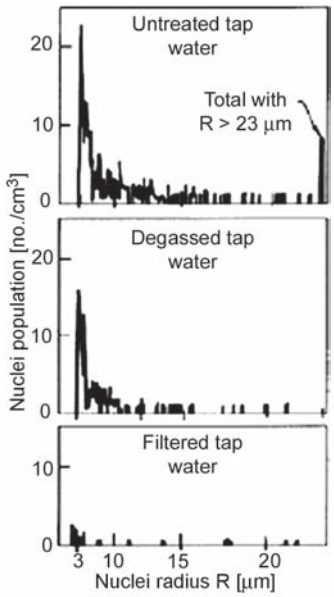


Fig. 7. Distribution of nuclei in water in three stages of degassing [1].

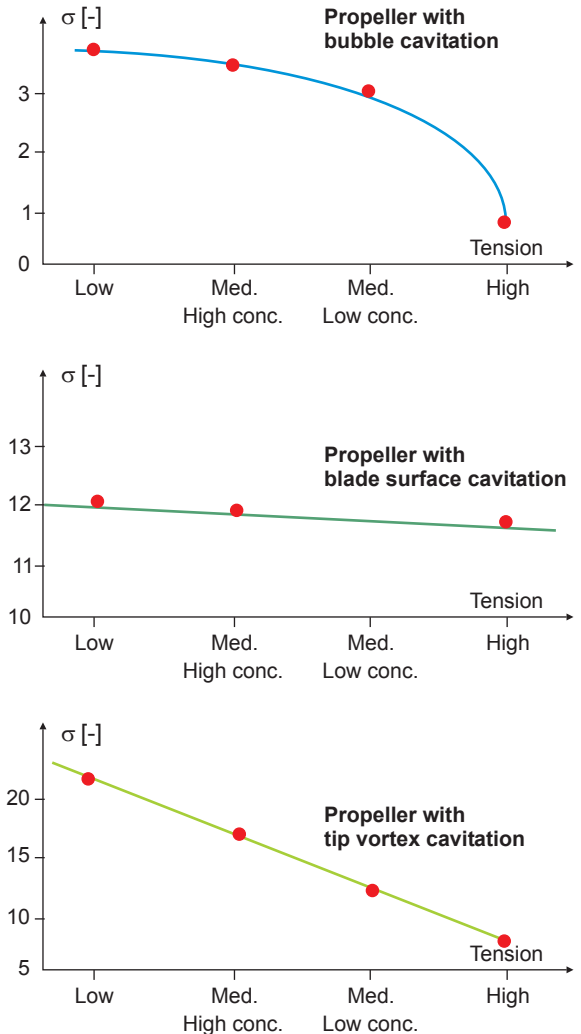


Fig. 8. Influence of the nuclei concentration on the inception cavitation number for three forms of cavitation [2].

The influence of dissolved air on the cavitation inception condition may be qualitatively illustrated by Fig.9 showing experimentally obtained curves for inception of tip vortex, hub vortex, sheet (surface) and bubble cavitation for two concentrations of dissolved air.

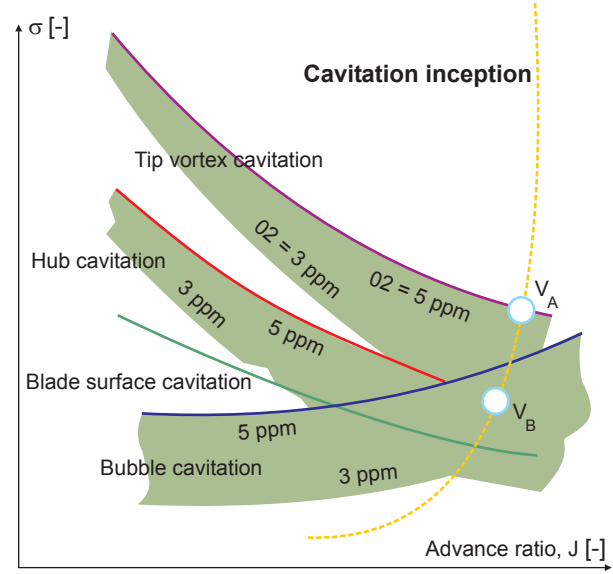


Fig. 9. Influence of dissolved air on cavitation inception on a marine propeller model [2].

The above described scale effect in cavitation experiments with marine propeller models is especially important for naval and other special applications. In these applications ensuring a completely cavitation-free operation is essential because of acoustic emission. It requires very precise knowledge about scale effects important for scaling cavitation inception condition. This implies, among other things, information about nuclei content in sea water. Measurements of such nuclei content were conducted for example by the French Navy [2]. Results of the assessment of sea water tensile strength at different depth are shown for example in Fig.10. These results may serve as certain guidance in scaling of the results of model experiments with marine propellers into full scale.

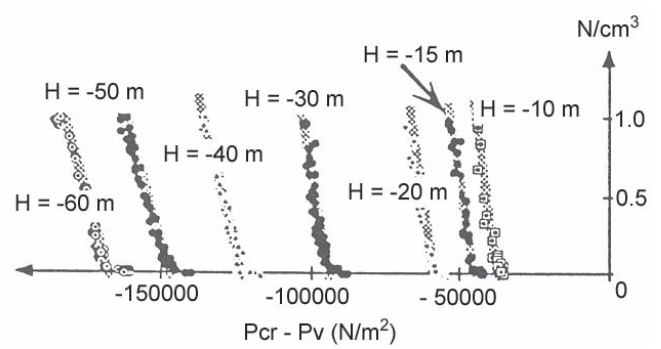


Fig. 10. Results of measurements of sea water tensile strength at different depths [2].

In case of typical cargo ship propellers it is generally accepted that routine guidelines for degassing water in cavitation tunnel and keeping the dissolved air content below about 30 per cent of saturation are sufficient to ensure the model cavitation test results corresponding to full scale situation. However, it is still important to know the nature of the scale effect due to the water quality.

THE EFFECT OF THE BOUNDARY LAYER PHENOMENA

The boundary layer phenomena depend primarily on the value of the Reynolds number. This number is composed of the characteristic velocity, characteristic dimension and viscosity coefficient. However, in the case of cavitation scaling it may be distinguished between Reynolds number effect (strictly linked to the boundary layer phenomena) and separate effects of the flow velocity and object size, which have a completely different physical mechanism and are discussed separately in the following sections.

In turn the “pure” Reynolds number effect may be divided into (1) a difference in quasi-steady pressure distribution between model scale and full scale propeller blades and (2) unsteady velocity/pressure fluctuations inside the boundary layer. The first of these two effects is of lesser importance, but nonetheless it should be taken into account. The limited relative importance of this effect may be assessed on the basis of lift-related scale effect corrections for marine propellers as discussed for example in [7].

The second effect is much more important, particularly from the point of view of cavitation inception scaling. According to [6] pressure fluctuations inside the boundary layer on a blade section profile may reach quite high amplitudes, comparable with the mean value of pressure in the vicinity of the leading edge. These fluctuations may be added to the distribution of mean pressure along the blade section profile.

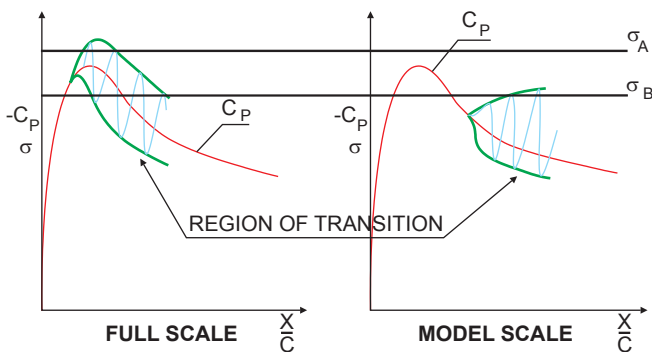


Fig. 11. Pressure fluctuations inside the boundary layer on a blade section in model scale and full scale.

These fluctuations reach maximum amplitudes in the region of laminar/turbulent transition. Due to the difference between model and full scale Reynolds numbers this region of transition is located differently on the model scale blade section profile and in corresponding full scale situation (cf. Fig.11). In full scale this region is located close to the leading edge, where the point of minimum of the mean pressure coefficient C_p is also located if the profile operates at an angle of attack. In model scale this region is located further downstream, where the mean pressure on the suction side of the profile is already markedly higher. Consequently, at the value σ_A of the local cavitation number inception may take place in full scale, but not in model scale. Typical frequency of pressure/velocity oscillation in the transition zone is of order 1 [kHz], while the own oscillation frequency of cavitation nuclei between 20 and 50 microns (most frequently encountered in real flows) is of order 50 [kHz]. From this we may conclude that any of these micro-bubbles reaching the laminar/turbulent transition zone will be destabilized by the pressure pulsations and may cause inception of cavitation. If the local cavitation number is sufficiently low, say equal to σ_B , inception and development of cavitation will be experienced both in full and model scale.

THE EFFECT OF THE TIME AND VELOCITY SCALES

It is generally accepted that inception of cavitation takes place when cavitation nuclei present in the flow are destabilized by the flow conditions and they undergo dynamic growth [5]. In order to achieve this, the nuclei must be acted upon by a sufficiently low pressure during a sufficiently long time. This situation is illustrated in Fig.12. In this figure C_p is the non-dimensional pressure distribution along a blade section profile and σ_1 means the theoretical cavitation inception number, based on the assumption $p_{CR} = p_v$. Due to the above described effect, the actual inception cavitation number will be lower and equal σ_1^T . It may be assumed that a certain value C of the multiple of mean pressure difference between local pressure and vapour pressure Δp and time Δt is required to initiate cavitation. This parameter C is inversely proportional to the typical size of cavitation nuclei (compare Eq. 6), so it may be assumed that its value is similar in model and full scale. Then the following relation may be developed:

$$C = \Delta p \Delta t = \frac{\rho}{2} V_0^2 \Delta C_p \frac{L}{V_0} \Delta \frac{x}{L} = \frac{\rho}{2} V_0 L \int_{x_1/L}^{x_2/L} (C_p - \sigma_1^T) d\left(\frac{x}{L}\right) \quad (7)$$

where :

- V_0 – characteristic velocity of flow at the blade section
- L – length of the blade section
- ΔC_p – non-dimensional pressure difference (cf. Fig.12).

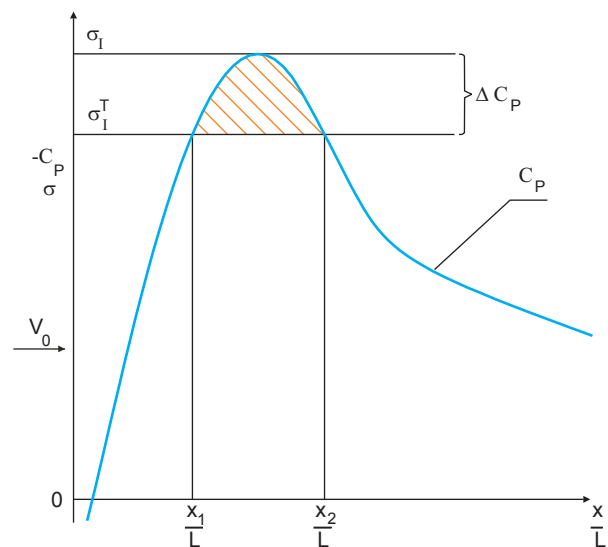


Fig. 12. The effect of time and pressure difference on cavitation inception.

The following observations may be made from the form of equation (7) :

- the same object tested at different velocities will have different values of the actual inception cavitation number σ_1^T ; this value will be smaller for smaller velocity; on the other hand it will be closer to σ_1 for larger velocity
- for two geometrically similar objects of different sizes tested at the same velocity the smaller object will exhibit smaller value of σ_1^T
- two geometrically similar objects of different sizes tested at the same value of $V_0 L$ will exhibit identical values of σ_1^T .

If the relation (7) is applied to the situation of the model and full scale marine propeller, it may be concluded that the characteristic velocity V_0 in full scale is about twice the model value and the characteristic length L in full scale is about 25 times the model value. Consequently, the actual inception cavitation number σ_1^T will be visibly higher in full scale than in model scale. As a result, cavitation inception in full scale may happen earlier than indicated by the model experiments. This effect may be illustrated by the photographs shown in Fig.13. In these photographs cavitation on the so called Schiebe body is shown at two different flow velocities but at the same value of the cavitation number.

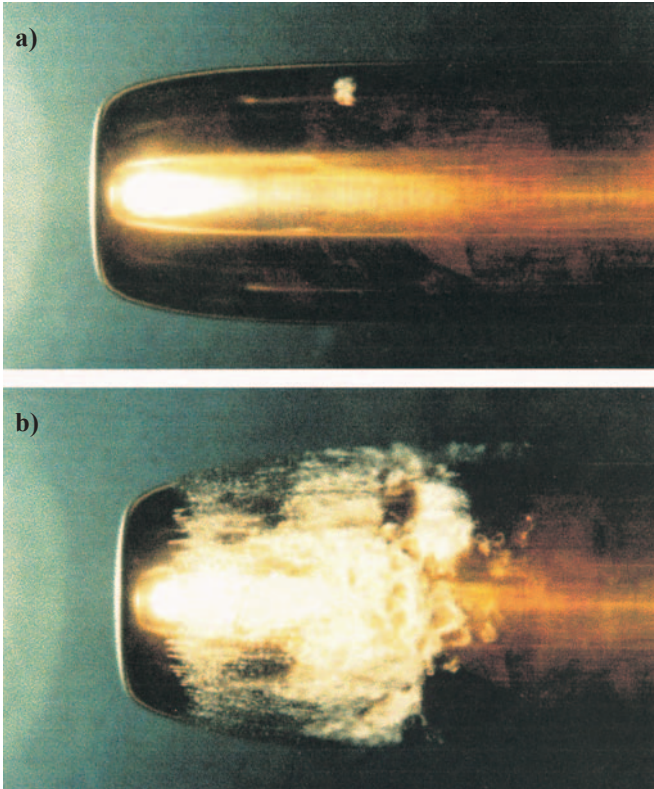


Fig. 13. Schiebe body tested at the same cavitation number but at $V_0 = 8$ [m/s] (a) and at $V_0 = 14$ [m/s] (b), quoted from [3].

THE EFFECT OF THE OBJECT SIZE

One could assume that if the scale effect due to the difference between model and full scale Reynolds number is properly taken into account, then there is no need to analyse separately the effect of object size. However, the complicated nature of cavitation leads to a separate scale effect of the object size. This may be justified by the following reasoning :

- ⇒ two geometrically similar objects of different sizes will exhibit similar regions of low pressure having size proportional to the object size
- ⇒ if the same distribution of the cavitation nuclei in the oncoming flow is assumed in both cases, then more nuclei will enter the low pressure region around the larger object
- ⇒ consequently, the probability of destabilization of nuclei and cavitation inception is higher for a larger object.

This effect may be illustrated by the photographs shown in Fig.14. However, it should be kept in mind that in the laboratory experiments there are always many different factors influencing the results at the same time. The results shown in Fig.14, but also in Fig.13 may be the joint consequence of effects mentioned in this section and in two preceding sections together.

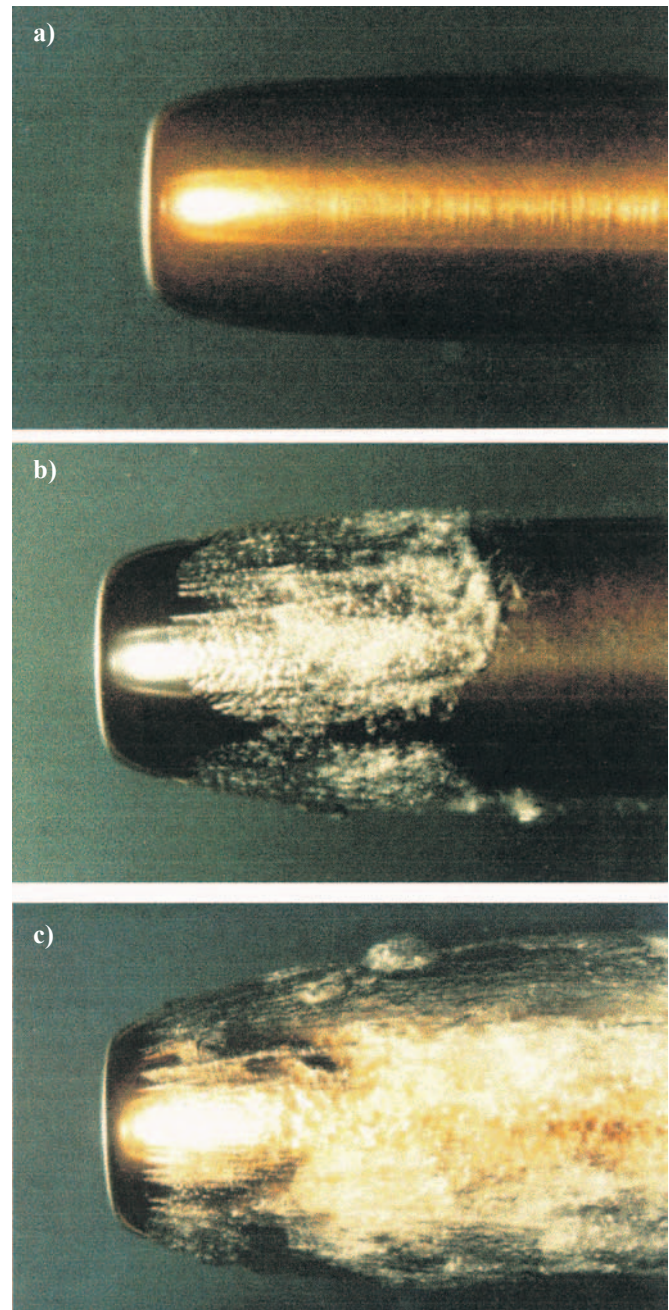


Fig. 14. Three geometrically similar Schiebe bodies of different sizes tested at the same cavitation number :
a) diameter 15 [mm], **b)** diameter 30 [mm],
c) diameter 60 [mm], quoted from [3].

CONCLUSION

The above presented analysis of the specific scale effects, influencing full scale predictions of the marine propellers cavitation behaviour made on the basis of model experiments, leads to the following conclusions :

- most of the specific scale effects are more important for inception of cavitation on marine propellers and less important for the fully developed cavitation phenomena; consequently, these scale effects are more important for design of “silent propellers” (naval, research, passenger ships etc.) than for routine cargo ships propellers
- the unavoidable effect of static pressure distribution may affect both inception and development of cavitation; it may also generate meaningful differences in the propeller induced pressure pulses; the influence of this scale effect

- may be minimized by proper selection of the cavitation number in model experiments
- the water quality effect, in particular the distribution of cavitation nuclei in the experimental facility and at sea, is the source of important scale effect on cavitation inception; at present it can not be fully taken into account during scaling of the model results due to the lack of information about true full scale situation
 - the boundary layer scale effect may lead to meaningful under-prediction of the cavitation inception condition in full scale
 - the velocity and time scale effect may also lead to under-prediction of the full scale cavitation inception condition
 - the effect of object size also points to a possibility of under-prediction of the full scale cavitation inception condition
 - consequently, the results of model experiments performed for prediction of cavitation inception on full scale propellers must be taken with special care and the designers should be aware of the fact that all specific scale effects cause the full scale propeller cavitation behaviour visibly less optimistic than indicated by model experiments.

NOMENCLATURE

c	- blade section chord length
C_p	- non-dimensional pressure coefficient
C_p^{\min}	- minimum value of the non-dimensional pressure coefficient
ΔC_p	- non-dimensional pressure difference
D	- propeller diameter
g	- acceleration of gravity
h	- immersion of point where cavitation number is defined
J	- propeller advance coefficient
L	- characteristic length
n	- propeller number of revolutions
p_A	- atmospheric pressure
Δp	- difference between local pressure and vapour pressure
p_{CR}	- critical pressure
p_I	- cavitation inception pressure
p_T	- tensile strength of the liquid
p_{TUN}	- pressure inside cavitation tunnel
p_V	- vapour pressure
R	- cavitation bubble radius
Re	- Reynolds number
S	- surface tension of water
Δt	- time necessary for cavitation inception
V	- propeller advance velocity
V_0	- characteristic velocity
V_R	- reference velocity
$\frac{x}{c}$	- non - dimensional coordinate along profile chord
θ	- propeller blade position angle
λ	- model scale coefficient
ν	- kinematic viscosity coefficient
ρ	- density of water
σ	- cavitation number
$\Delta\sigma$	- change in cavitation number due to tensile strength of water
σ_1	- inception cavitation number
σ_1^T	- inception cavitation number including water tensile strength

BIBLIOGRAPHY

1. Brennen C.E.: *Cavitation and Bubble Dynamics*. Oxford University Press. 1995
2. Gindroz B., Billet M.L.: *Nuclei and Acoustic Cavitation Inception of Ship Propellers*. Proc. 2nd Int. Symposium on Cavitation. Tokyo, Japan. 1994

3. Keller A.P.: *Cavitation Scale Effects – A Representation of its Visual Appearance and Empirically Found Relations*. Proc. Intern. Conference NCT'50, Newcastle-upon-Tyne. 2000
4. Keller A.P.: *New Scaling Laws for Hydrodynamic Cavitation Inception*. Proc. 2nd Int. Symposium on Cavitation. Tokyo, Japan. April 1994
5. Knapp R.T., Daily J.W., Hammit F.G.: *Cavitation*, Mc Graw Hill. 1970
6. Schlichting H.: *Grenzschicht Theorie*. Verlag G. Braun. Karlsruhe. 1965
7. Szantyr J.: *Lift Based Propeller Scale Effect and Its Influence on Propulsive Characteristics of Ships*. Trans. West Japan Soc. Of Naval Architects No. 84(1992)

CONTACT WITH THE AUTHOR

Jan A. Szantyr, Prof. D. Sc., Ph. D. (Nav. Arch.)
 Department of Turbomachinery
 and Fluid Mechanics,
 Gdańsk University of Technology
 Narutowicza 11/12
 80-958 Gdańsk, POLAND
 e-mail : jas@pg.gda.pl

Miscellanea



TOP KORAB in 2005



Every year the Polish Society of Naval Architects and Marine Engineers, TOP KORAB, traditionally arranges, apart from its current activity, open meetings during which are discussed topics in advance announced dealing with shipbuilding and maritime economy.

In the year 2005 the following problems were dealt with by **Gdańsk Division of the Society** :

- ★ Prospects of Polish shipbuilding industry in taking advantage from the current boom in the worldwide market
- ★ Drilling unit equipment made in Poland
- ★ Fuel system blocks for ship diesel engines
- ★ The fastest-in-the-world computers and their technological trends
- ★ To day and to morrow of the firm Hydrobudowa S.A.

And in **Szczecin Division of the Society** :

- ★ Optimization models for engineering and economy
- ★ Organization of the Conference on : Past, present and future state of Polish shipbuilding industry

In 2005 the most important event for the Society was the signing of the agreement on establishment of RINA/KORAB Joint Branch. The agreement was signed on behalf of TOP KORAB by B. Banach, its Chairman and J. Czuczman, its Vice-chairman, and on behalf of RINA by T. Blakeley, RINA Chairman. The document was also signed by Prof. J. W. Doerffer, Honorary Member of TOP KORAB, Fellow Member of RINA.

Effective fatigue damage summation

Janusz Kolenda

Gdańsk University of Technology
Polish Naval University



The cumulative fatigue damage caused by uniaxial variable stress is considered. To facilitate the lifetime prediction at complex stress patterns, has been defined an effective stress of constant parameters, claimed to be equivalent to the sequence of original stresses in terms of fatigue life of material. The equivalence conditions are based on the theory of energy transformation systems. To the effective stress the Palmgren-Miner rule is applied. Thereby the cycle counting is not required.

ABSTRACT

Keywords : fatigue, design criteria, damage cumulation, stress modeling

INTRODUCTION

Most engineering components are subjected to variable loading. The fatigue damage in materials under cyclic loads of variable level, direction and/or mode, is accumulated at an unsteady rate. Though many cumulative damage theories have been developed, none of them enjoys universal acceptance. Each fatigue damage model can only account for one or several phenomenological factors, such as load dependence, multiple damage stages, non-linear damage evolution, load sequence and interaction effects, mean stress, overload effects and small amplitude cycles below fatigue limit. The most convenient is the Palmgren-Miner rule [1,2], and it has been adopted and used extensively, mainly because of its simplicity. According to the original concept :

- ✓ the fatigue process is cumulative,
- ✓ the fatigue effect is proportional to the work done by active loads,
- ✓ the increment of damage caused by n stress cycles of constant amplitude can be estimated as n/N , where N is the number of stress cycles which would cause failure of material in the same load state.

As to the loads of variable amplitude, the concept holds that the total damage can be estimated as the sum of the damage increments, each corresponding to a specified stress level. This can be symbolically expressed by the equation :

$$D = \sum_{j=1}^w \frac{n_j}{N_j} \quad (1)$$

where :

- D - total fatigue damage which equals unity at the failure
- n_j - number of stress cycles at j -th stress level
- N_j - number of cycles to failure at j -th stress level
- w - number of stress levels.

The quantity N_j can be calculated as follows [3] :

$$N_j = \frac{K}{\sigma_j^m} \left(1 - \frac{\sigma_{mj}}{R}\right)^m \quad (2)$$

where :

- K - fatigue strength coefficient
(in equation of relevant S-N curve)
- m - fatigue strength exponent
- R - yield strength - for ductile materials,
ultimate strength - for brittle materials
- σ_j - stress amplitude at j -th stress level
- σ_{mj} - mean stress at j -th stress level.

Similar approach is applied to loads of variable level, direction and mode, namely :

$$D = \sum_i \sum_{j=1}^{w_i} \frac{n_{ij}}{N_{ij}} \quad ; \quad i = x, y, z, xy, yz, zx \quad (3)$$

where the indices $i = x, y, z$ are associated with normal stresses, and $i = xy, yz, zx$ with shear stresses in Cartesian coordinate system.

The Palmgren-Miner rule implicitly assumes that the damage cumulation is independent of the order in which the stress cycles of different levels are applied and of the order of load modes. The assumptions have been found inadequate in certain cases [4]. Moreover, the cycle counting may be a source of uncertainties and D values may differ significantly from unity at the failure. Therefore several other cumulative damage hypotheses have been proposed [5] but their applicability varies from case to case. In this context a relatively simple approach based on the Palmgren-Miner rule and effective stress models, can be mentioned. Such approach for zero mean variable stresses has been presented in [6]; it will be used below for nonzero mean variable stresses.

EFFECTIVE STRESS

In accordance with the theory of energy transformation systems [7] the following can be stated.

An effective stress model and an original stress can be regarded equivalent in terms of fatigue life of material if during its service life the internally and externally dissipated energies under effective and original stresses are equal, respectively.

To illustrate the determination of the effective stress, let us consider a variable stress of i -th mode in the high-cycle fatigue regime :

$$\tilde{\sigma}_j(t) = \sigma_{mj} + \sigma_j(t) ; j = 1, 2, \dots, w \quad (4)$$

where $\sigma_j(t)$ is a zero mean time-varying stress.

The sequence of stresses (4) can be modeled by the effective stress :

$$\tilde{\sigma}_e(t) = \sigma_{me} + \sigma_e \sin \omega_e t \quad (5)$$

where σ_{me} , σ_e and ω_e are its mean value, amplitude and circular frequency, respectively. The equivalence conditions corresponding to the above given statement are [6] :

$$\int_0^T \tilde{\sigma}_e^2(t) dt = \sum_{j=1}^w \int_0^{t_j} \tilde{\sigma}_j^2(t) dt \quad (6)$$

$$\int_0^T \dot{\tilde{\sigma}}_e^2(t) dt = \sum_{j=1}^w \int_0^{t_j} \dot{\tilde{\sigma}}_j^2(t) dt \quad (7)$$

where :

t_j - the duration of j -th load state, dot denotes differentiation with respect to time, and T :

$$T = \sum_{j=1}^w t_j \quad (8)$$

Eqs (6) and (7) determine parameters of the effective stress.

For example, when :

$$\tilde{\sigma}_j(t) = \sigma_{mj} + \sigma_j \sin \omega_j t ; j = 1, 2, \dots, w \quad (9)$$

these equations yield :

$$\begin{aligned} \sigma_{me} &= \left[\frac{1}{T} \sum_{j=1}^w t_j \sigma_{mj}^2 \right]^{1/2} \\ \sigma_e &= \left[\frac{1}{T} \sum_{j=1}^w t_j \sigma_j^2 \right]^{1/2} \\ \omega_e &= \left[\frac{\sum_{j=1}^w t_j \omega_j^2 \sigma_j^2}{\sum_{j=1}^w t_j \sigma_j^2} \right]^{1/2} \end{aligned} \quad (10)$$

In Eq (9) σ_j is the stress amplitude and ω_j - the stress circular frequency at j -th level.

FATIGUE DAMAGE

On determination of the effective stress parameters and the number of stress cycles during w load states of i -th mode :

$$n_e = \frac{\omega_e}{2\pi} T \quad (11)$$

the following is postulated :

- the fatigue process at the effective stress is cumulative,
- the fatigue effect is proportional to the dissipative energy,
- the increment of damage, corresponding to n_e cycles of the effective stress, can be estimated as follows :

$$D_e = \frac{n_e}{N_e} = D_{ei} \quad (12)$$

where :

$$N_e = \frac{K}{\sigma_e^m} \left(1 - \frac{\sigma_{me}}{R} \right)^m \quad (13)$$

Additionally, if the load is variable then the total fatigue damage based on the concept of the effective stress is assumed to be :

$$D_e = \sum_i D_{ei} ; i = x, y, \dots, zx \quad (14)$$

Of course, with the presented approach the aforementioned drawback of the Palmgren-Miner rule, associated with ignoring the load sequence effects, cannot be avoided, but the cycle counting is not required.

EXAMPLE

Task :

- ❖ Compare the cumulative fatigue damages D and D_e if the load is of i -th mode and the stress sequence consists of n_i cycles of the stress :

$$\tilde{\sigma}_1(t) = \sigma_{m1} + \sigma_1 \sin \omega_1 t$$

and n_2 cycles of the stress :

$$\tilde{\sigma}_2(t) = \sigma_{m2} + \sigma_2 \sin \omega_2 t$$

in the high-cycle fatigue regime when :

$$\frac{\sigma_{mj}}{R} + \frac{\sigma_j}{F} > 1 \geq \frac{\sigma_{mj}}{R} + \frac{\sigma_j}{L} ; j = 1, 2$$

where :

F - the fatigue limit under fully reversed stress of i -th mode

L - the maximum stress amplitude σ satisfying equation of i -th S-N curve

$$N\sigma^m = K$$

above which the low-cycle fatigue may occur.

- ❖ Consider the following cases :

$$A : n_1 = n_2 = n ; \sigma_{m1}/R = 0.5 ; \sigma_{m2}/R = 0.5\gamma$$

$$\sigma_1 = \sigma_2 = \sigma ; \omega_1 = \omega_2 = \omega$$

$$B : n_1 = n_2 = n ; \sigma_{m1} = \sigma_{m2} = \sigma_m$$

$$\sigma_2 = \gamma\sigma_1 ; \omega_1 = \omega_2 = \omega$$

$$C : n_1 = n_2 = n ; \sigma_{m1} = \sigma_{m2} = \sigma_m$$

$$\sigma_2 = \sigma_1 = \sigma ; \omega_2 = \gamma\omega_1$$

Solution :

A. According to the Palmgren-Miner rule and Eq.(2), the fatigue damage D equals :

$$D = \frac{n_1}{N_1} + \frac{n_2}{N_2} = n \left(\frac{1}{N_1} + \frac{1}{N_2} \right)$$

where :

$$N_1 = \frac{K}{\sigma_m} (1 - 0.5)^m ; N_2 = \frac{K}{\sigma_m} (1 - 0.5\gamma)^m$$

The parameters of the effective stress are calculated from Eqs (10) for $t_1 = t_2 = 0.5T$, as follows :

$$\frac{\sigma_{me}}{R} = \left[\frac{1}{T} \left(t_1 \frac{\sigma_{m1}^2}{R^2} + t_2 \frac{\sigma_{m2}^2}{R^2} \right) \right]^{1/2} = \left[0.125(1 + \gamma^2) \right]^{1/2}$$

$$\sigma_e = \left[\frac{1}{T} (t_1 \sigma_1^2 + t_2 \sigma_2^2) \right]^{1/2} = \sigma$$

$$\omega_e = \left[\frac{t_1 \omega_1^2 \sigma_1^2 + t_2 \omega_2^2 \sigma_2^2}{t_1 \sigma_1^2 + t_2 \sigma_2^2} \right]^{1/2} = \omega$$

Since the load duration is :

$$T = \frac{2\pi}{\omega_1} n_1 + \frac{2\pi}{\omega_2} n_2 = \frac{4\pi}{\omega} n$$

the number of cycles of the effective stress amounts to :

$$n_e = \frac{\omega_e}{2\pi} T = 2n$$

and the number of its cycles to failure is :

$$N_e = \frac{K}{\sigma_e^m} \left(1 - \frac{\sigma_{me}}{R} \right)^m = \frac{K}{\sigma_m^m} \left\{ 1 - \left[0.125(1 + \gamma^2) \right]^{1/2} \right\}^m$$

Hence

$$D_e = \frac{2n\sigma^m}{K \left\{ 1 - \left[0.125(1 + \gamma^2) \right]^{1/2} \right\}^m}$$

and

$$\frac{D}{D_e} = 0.5 \left[\frac{1}{0.5^m} + \frac{1}{(1 - 0.5\gamma)^m} \right] \cdot \left\{ 1 - \left[0.125(1 + \gamma^2) \right]^{1/2} \right\}^m \quad (15)$$

The results of the exemplary calculation of the ratio D/D_e are given in Tab. 1.

Tab. 1. Results of calculation with the use of Eq. (15).

m	3				
γ	0.6	0.8	1.0	1.2	1.4
D/D_e	1.11	1.03	1.00	1.06	1.35
m	6				
γ	0.6	0.8	1.0	1.2	1.4
D/D_e	1.49	1.15	1.00	1.24	2.58

B. In the case of variable amplitude stress one obtains :

$$D = n \left(\frac{1}{N_1} + \frac{1}{N_2} \right)$$

where :

$$N_1 = \frac{K}{\sigma_1^m} \left(1 - \frac{\sigma_m}{R} \right)^m ; N_2 = \frac{K}{(\gamma\sigma_1)^m} \left(1 - \frac{\sigma_m}{R} \right)^m$$

The parameters of the effective stress are :

$$\sigma_{me} = \left[\frac{1}{T} (0.5T\sigma_m^2 + 0.5T\sigma_m^2) \right]^{1/2} = \sigma_m$$

$$\sigma_e = \left[\frac{1}{T} (0.5T\sigma_1^2 + 0.5T\gamma^2\sigma_1^2) \right]^{1/2} = \left[0.5(1 + \gamma^2) \right]^{1/2} \sigma_1$$

$$\omega_e = \left[\frac{0.5T\omega^2\sigma_1^2 + 0.5T\omega^2\gamma^2\sigma_1^2}{0.5T\sigma_1^2 + 0.5T\gamma^2\sigma_1^2} \right]^{1/2} = \omega$$

so that :

$$N_e = \frac{K}{\left[0.5(1 + \gamma^2) \right]^{m/2} \sigma_1^m} \left(1 - \frac{\sigma_m}{R} \right)^m$$

and

$$\frac{D}{D_e} = \frac{n \left(\frac{1}{N_1} + \frac{1}{N_2} \right)}{\frac{2n}{N_e}} = \frac{1 + \gamma^m}{2 \left[0.5(1 + \gamma^2) \right]^{m/2}} \quad (16)$$

Exemplary values of D/D_e are presented in Tab. 2.

Tab. 2. Results of calculation with the use of Eq. (16).

m	3				
γ	0.6	0.8	1.0	1.2	1.4
D/D_e	1.08	1.02	1.00	1.01	1.04
m	6				
γ	0.6	0.8	1.0	1.2	1.4
D/D_e	1.66	1.26	1.00	1.10	1.32

C. In Tab. 3 the values of the ratio D/D_e are presented as calculated for the stress of variable frequency at different relative frequency ranges :

$$\frac{\Delta\omega}{\omega_m} = \frac{|1 - \gamma|}{\sqrt{\gamma}}$$

Here

$$\Delta\omega = |\omega_1 - \omega_2|$$

is the difference between higher and lower circular frequency of the stresses $\bar{\sigma}_1(t)$ and $\bar{\sigma}_2(t)$, and :

$$\omega_m = \sqrt{\omega_1 \omega_2}$$

is the central circular frequency of the stress cycles.

For the period :

$$T = t_1 + t_2 = \frac{2\pi}{\omega_1} n_1 + \frac{2\pi}{\omega_2} n_2 = \frac{2\pi n}{\omega} \left(1 + \frac{1}{\gamma} \right)$$

the parameters of the effective stress are :

$$\sigma_{me} = \sigma_m ; \sigma_e = \sigma ; \omega_e = \sqrt{\gamma} \omega$$

and the number of its cycles is :

$$n_e = \frac{\omega_e}{2\pi} T = \frac{1 + \gamma}{\sqrt{\gamma}} n$$

By applying Eqs (2) and (13), the number of cycles to failure under considered stresses is the same, namely :

$$N_1 = N_2 = N_e = \frac{K}{\sigma_m^m} \left(1 - \frac{\sigma_m}{R} \right)^m$$

Consequently :

$$\frac{D}{D_e} = \frac{2n}{n_e} = \frac{2\sqrt{\gamma}}{1+\gamma} \quad (17)$$

Tab. 3. Results of calculation with the use of Eq. (17).

γ	0.2	0.4	0.6	0.8	1.0	1.2
$\Delta\omega/\omega_m$	1.79	0.95	0.52	0.22	0.00	0.18
D/D_e	0.75	0.90	0.97	0.99	1.00	1.00
γ	1.4	1.6	1.8	2.0	4.0	10.0
$\Delta\omega/\omega_m$	0.34	0.47	0.60	0.71	1.50	2.85
D/D_e	0.99	0.97	0.96	0.94	0.80	0.57

From Tab. 1, 2 and 3 it can be observed that the linear summation of the fatigue damage corresponding to the effective stress, based on the theory of energy transformation systems, leads to less conservative results for the stresses of variable level (in particular at higher values of the fatigue strength exponent), and to even more conservative results for the stresses of variable frequency (especially at the relative frequency ranges greater than unity). The observed discrepancies between the values of the fatigue damages D and D_e result from different assumptions concerning the work of the active loads in the Palmgren-Miner rule and the dissipative energy in the equivalence conditions (6) and (7).

CONCLUSIONS

- For majority of engineering components, fatigue process under service conditions involves variable loading history. The cycle counting technique and the Palmgren-Miner rule are then frequently used for fatigue lifetime prediction. However, at complex stress patterns the cycle counting procedure may be complicated.
- The effective stress defined in the foregoing text, makes it possible to avoid this difficulty if the stress process is integrable in respect of time over the service period.
- From the exemplary calculations it follows that the linear summation of fatigue damages corresponding to the effective stress leads to less conservative results than that corresponding to the original stress of variable level, and to even more conservative results when the frequency of the original stress is variable.

NOMENCLATURE

- D - fatigue damage
- D_e - fatigue damage corresponding to the effective stress
- D_{ei} - fatigue damage corresponding to the effective stress of i -th mode ($i=x,y,z, xy, yz, zx$)
- F - fatigue limit under fully reversed stress
- K - fatigue strength coefficient
- L - maximum stress amplitude satisfying equation of the S-N curve above which the low-cycle fatigue may occur
- m - fatigue strength exponent
- n - number of stress cycles
- n_e - number of the effective stress cycles
- n_j - number of stress cycles at j -th level
- n_{ij} - number of stress cycles of i -th mode at j -th level
- N - number of zero mean stress cycles
- N_e - number of the effective stress cycles to failure
- N_j - number of stress cycles to failure at j -th level

- N_{ij} - number of stress cycles to failure at i -th mode and j -th level
- R - yield strength - for ductile materials, ultimate strength - for brittle materials
- t - time
- t_j - duration of j -th load state
- T - duration of w load states
- w - number of stress levels
- w_i - number of levels of i -th mode stress
- γ - multiplying factor
- σ - stress amplitude
- σ_e - amplitude of the effective stress
- $\tilde{\sigma}_e(t)$ - effective stress
- σ_j - amplitude of the stress $\tilde{\sigma}_j(t)$ in Eq. (9)
- $\tilde{\sigma}_j(t)$ - zero mean time-varying stress of j -th level
- $\tilde{\sigma}_j(t)$ - variable stress of j -th level
- σ_m - mean value of the stress
- σ_{me} - mean value of the effective stress
- σ_{mj} - mean value of the stress $\tilde{\sigma}_j(t)$
- ω - circular frequency
- ω_e - circular frequency of the effective stress
- ω_j - circular frequency of the stress $\tilde{\sigma}_j(t)$ in Eq. (9)

BIBLIOGRAPHY

1. Palmgren A.: *Die Lebensdauer von Kugellagern*. Verfahrenstechnik, 68, 1924
2. Miner M.A.: *Cumulative damage in fatigue*. *Journal of Applied Mechanics*, 67, 1945
3. Kolenda J.: *On fatigue safety of metallic elements under static and dynamic loads*. Gdańsk University of Technology Publishers, Gdańsk, 2004
4. Lin H., Nayeb-Hashemi H., Berg C.A.: *Cumulative damage behavior of anisotropic Al-6061-T6 as a function of axial-torsional loading mode sequence*. *J. Engng Materials and Technology*, 1, 1999
5. Fatemi A., Yang L.: *Cumulative fatigue damage and life prediction theories: a survey of the state of the art for homogeneous materials*. *Int. J. Fatigue*, 1, 1998
6. Kolenda J.: *Analytical procedures of high-cycle fatigue assessment of structural steel elements*. Gdańsk University of Technology Publishers, Gdańsk, 1997
7. Cempel C.: *Theory of energy transformation systems and their application in diagnostic of operating systems*. *Applied Math. and Computer Sciences*, 3, 1993.

CONTACT WITH THE AUTHOR

Prof. Janusz Kolenda
Faculty of Ocean Engineering
and Ship Technology,
Gdańsk University of Technology
Narutowicza 11/12
80-952 Gdańsk, POLAND
e-mail : sek7oce@pg.gda.pl



Main building of Gdańsk University of Technology

Photo : Cezary Spigarski

Processing methods of measured runs of torque and angular speed of combustion engine propulsion system

Stanisław Polanowski
Polish Naval University

ABSTRACT



In this paper four processing methods of cyclic data runs, namely : Fourier interpolation and transformation, least-squares approximation by means of trigonometric polynomials , synchronous averaging and movable approximation , were presented by using, as an example, discretely measured runs of torque and angular speed. It was demonstrated that for extracting a useful signal out of disturbance background and decomposing the disturbances the appropriate methods are the synchronous averaging and multiple movable approximation.

To emerge significant spectral lines from a spectrum the least-squares approximation by using trigonometric polynomials can be applied. The method contains a criterion for signal filtration and is insensitive to disturbances, run truncation and sampling irregularity. Fast Fourier Transform (FFT) may have an auxiliary significance for preliminary spectral analysis. Its main disadvantage is that in order to build a smoothing-out filter its parameters should be determined in advance, e.g. by applying one of the remaining methods.

Keywords : Ship piston engine, torque, angular velocity, data processing, Fast Fourier Transform (FFT), least-squares approximation by using trigonometric polynomials (TLSA), movable approximation, synchronous averaging.

INTRODUCTION

A convenient source of diagnostic information about work of ship combustion engine cylinders may be the torque measured on shafts of propulsion systems and angular speed measured by using proximity detectors placed over flywheels and free ends of shafts or other elements kinematically connected with engine crankshaft. In runs of the above mentioned quantities an information about work of all cylinders and entire propulsion system is aggregated that is why they are interesting from the point of view of possible gaining a diagnostic information from them. On the torque and angular speed runs natural vibrations of propulsion system and its elements, variations of consumer's power demand and technical state changes of propulsion system are superimposed. Runs of the above specified quantities are characterized by periodicity which results from cyclic work of piston engines. Sampling is timed by pulses coming from angular position of crankshaft.

Searching for different symptoms in measurement series including those of technical state changes requires applying mathematical tools for making it possible to extract useful signals out of the background of other signals and disturbances.

INTERPOLATION AND APPROXIMATION OF RUNS BY MEANS OF TRIGONOMETRIC POLYNOMIALS

Essence of Fourier interpolation and transformation

In order to highlight differences in results of data processing realized by using other methods it seems reasonable to remind in this work that the crucial element of Fourier interpolation is expansion of the periodic function with the period T :

$$f(\tau) = f(\tau + kT) \quad k = 1, 2, 3, \dots$$

into the infinite trigonometric series of the form :

$$f(\tau) = \frac{a_0}{2} + \sum_{k=1}^{\infty} (a_k \cos 2\pi v_k \tau + b_k \sin 2\pi v_k \tau) \quad (1)$$

where : $v_k = k/T$ – frequency.

The constant a_0 and coefficients a_k and b_k are determined by means of commonly known integral formulae. Dimension of the argument τ results from physical phenomena represented

by a measured run and is usually considered identical with time or axis of natural numbers ordering the set of samples of measurement series.

Eq. (1) can be expressed in the following form :

$$f(\tau) = A_0 + \sum_{k=1}^{\infty} A_k \cos(2\pi v_k \tau - \Phi_k) \quad (2)$$

$$A_0 = \frac{a_0}{2} ; A_k = \sqrt{a_k^2 + b_k^2} ; \Phi_k = \text{arctg}\left(\frac{b_k}{a_k}\right) \quad (3)$$

where :

A_0 – constant (mean value of series)

A_k, Φ_k – amplitude and phase of n -th spectral line, respectively, [2].

Ordered runs of the quantities A_n and Φ_n constitute spectra (images) of amplitudes and phases of a considered run in frequency domain and are Fourier transformation of the analyzed run. Initial run can be reconstructed by means of Fourier inverse transformation. Filtration in frequency domain is realized by means of relevant operations on spectra e.g. by multiplying a given spectrum by suitably selected weighting functions prior to making the inverse transformation. In particular if some spectral lines or their groups are removed it will constitute a frequency filtration.

Generally the function $f(\tau)$ and its image are considered in complex domain. Transition to the complex form is based on the known Euler formula [2]. In this work to apply the complex description was not necessary. However its knowledge is necessary in the case of making use of a software for determining transforms where results are given only in the complex form, e.g. as in Excel software.

The Discrete Fourier Transform (DFT) concerns the transformation of discrete data series described with the finite constant sampling period $\Delta\tau$ where form of the sampled function is no longer known, that means that to shorten sampling period, if required, is not possible. If a series is finite (i.e. it contains N samples) then the series corresponds with the measurement series.

The idea of transformation maintains unchanged and in this case it consists in interpolation of series by means of trigonometric polynomials, as shown above.

In connection with the transition from continuous function to its discrete representation, two problems arose already in theoretical phase: of Nyquist frequency and of aliasing [1, 2].

In 1918 H. Nyquist announced that $2v_g T$ samples are sufficient for approximate representing the signal whose spectrum is limited by the frequency v_g , and duration time is T . In 1949 K. C. E. Shannon published the proof of the theorem on run sampling and that on run reconstruction [2]. The Shannon theorem on run sampling cannot be expressed in a simple way and it is better to make use of the Shannon theorem on run reconstruction, which states that if for the sampling frequency v the relationship $v \geq v_g$ is fulfilled then the function $f(\tau)$ is unambiguously reproducible on the basis of its discrete values [2]. In practice are applied greater sampling frequencies depending on sampling purpose [2] since for reproduction of a given function a sufficiently complex Shannon's interpolation polynomial should be used and that the sampling process parameters do not satisfy the assumptions of Dirac's pulse comb function.

When a run whose spectrum contains spectral lines of frequencies greater than v_g is sampled with the frequency v_g then the aliasing phenomenon will occur [1, 2]. In order to be protected against this phenomenon, during measurements low-pass filters or, if possible, a sampling frequency increased

up to a safe value, is applied. As possible recording is limited only to finite representations of the investigated measurement runs the next problem arises, namely that of leak which consists in appearing, in a given spectrum, not existing spectral lines resulting from cutting-off sinusoidal components. Therefore it follows that the interval of measured series does not constitute an integral multiple of every sinusoidal component. An entire branch of mathematics and measurement engineering has been developed to elaborate suitable time filters (windows) to mitigate influence of the phenomenon on derived frequency spectrum [1, 2].

In the domain of practical computer-based spectral analyses the basic notion is Fast Fourier Transform (FFT). From the point of view of transformation theory the essence the FFT does not differ from that of the DFT. All the above given comments dealing with the DFT remain valid. In some elaborations any distinction between the DFT and FFT is not introduced [2]. The FFT problem consists in the computation algorithms owing to which it has been possible to greatly decrease number of main computational operations. Many kinds of FFT software have been developed. Cooley and Tukey, who presented their algorithm [6] in 1965, are regarded as the authors of the computer-based FFT.

The FFT software is offered in many recognized program packets such as e.g. Matlab, Mathematica, Excel. They may differ from each other in different algorithms for determining the FFT, and results obtained by means of different programs may appear not identical for some parameters of the same data sets.

Analysis of results of measurements of torque and angular speed runs with the use of the FFT

Transforms of example measurement series and several its testing modifications were determined in order to compare features of the analysis of measured runs made by using the FFT and least-squares approximation with application of trigonometric polynomials. To this end was used the torque and angular speed runs (shown in Fig. 1) measured on a real object.

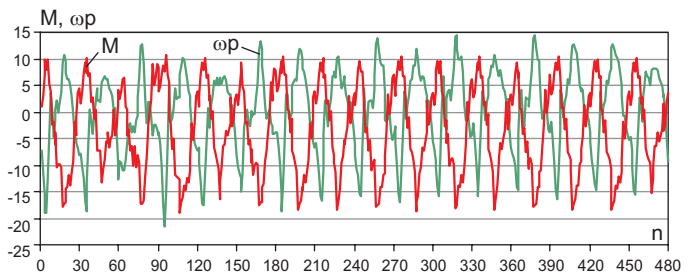


Fig. 1. Measured runs obtained by means of a photo-electric speed indicator : M – torque (dimensionless), ω_p [rad/s \times 20] – angular speed pulses related to its mean value.

The above presented measurement results were obtained by means of the experimental unit of photo-electric disc torque meter of ENAMOR [4], on the test bed of one-cylinder two-stroke combustion engine [3]. From every shaft rotation 30 samples of both torque and angular speed were derived in the domain of shaft rotation angle, that results from the torque meter construction. Values of the torque M were left dimensionless as it does not matter for discussion on run processing. This example is interesting since characteristic symptoms and disturbances are distinctly present in the measured runs, especially those of the torque M .

The amplitude spectrum of the run of the torque M , determined by means of the FFT nested in Matlab, is shown in Fig. 2.

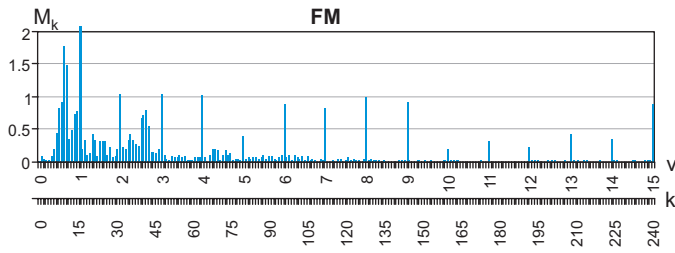


Fig. 2. The amplitude spectrum (FM) of the run of the torque M (Fig.1) derived by using Matlab software; M_k – amplitude of spectral lines, v – frequency; k – FFT natural axis (numbers of spectral lines).

Majority of FFT programs (among them also Matlab and Excel) take measurement input data as complex numbers. In such case the number of symmetrical spectral lines $N = 2K$ where N – number of samples of measurement series, and a constant is calculated. In the considered case where $N = 480$, apart from the constant, just 480 values of amplitudes and phases, 240 out of which constitute real values, are calculated. There are programs where only real values are determined. Phase spectra are not presented in this work as they are deemed useless for presentation and discussion of the problems in question.

To illustrate the symptoms which appear in results of real measurement data processing with the use of the FFT, was determined the test run M_T whose amplitude spectrum QM_T is shown in Fig.3.

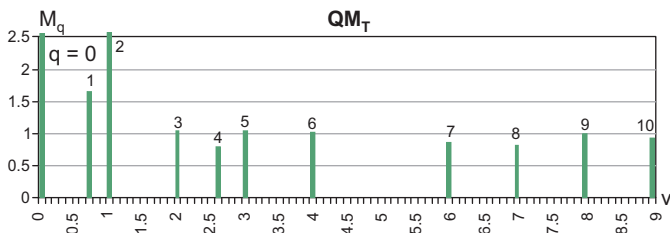


Fig. 3. The amplitude spectrum QM_T of the test run M_T , determined by applying the least-squares approximation method to the run M (Tab.1) : $M_0 = 3.1$; $M_2 = 10.46$.

The spectral lines of the spectrum (Fig.1) were obtained by using the least-squares approximation of the run M (Tab.1). In the figures spectral lines for $v > 9$ as well as those of small amplitude values were omitted in order to obtain better quality of imaging the spectra. Only 10 spectral lines were left due to which it was possible to better demonstrate influence of some factors on transformation results.

The amplitude FFT of the M_T test run, achieved by using the Matlab software is shown in Fig.4.

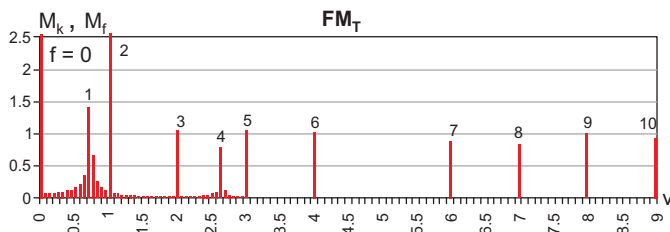


Fig. 4. The amplitude spectrum FM_T (FFT) of the M_T test run, obtained by means of the Matlab software.

As compared with the spectrum QM_T (Fig.3) in the spectrum FM_T (Fig.4) characteristic side spectral lines (stripes) appeared at non-integral frequencies.

The next test run, M_{TD} , was formed by removing 10 samples from each its end. The M_{TD} run contains $N = 460$ samples.

The FFT (obtained by using Matlab) is characterized by a much greater number of side spectral lines (stripes) especially in the range of low frequencies (Fig.5).

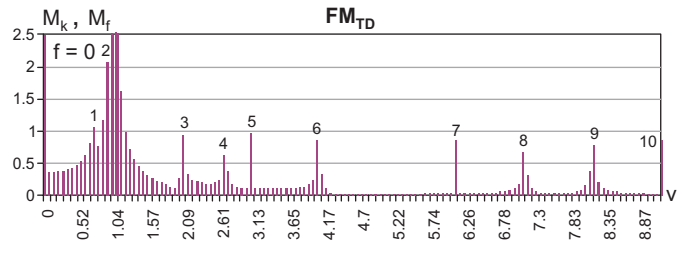


Fig. 5. The amplitude spectrum FM_{TD} of the M_{TD} test run, obtained by means of Matlab software; M_{TD} – the run formed from M_T run by removing 10 samples from each its end.

The phenomenon may constitute an obstacle in searching for characteristic spectral lines of lower amplitudes. Such cases can be met in measuring practice. Runs recorded without synchronizing and controlling pulses of starting-up and stopping the measurements will be generally truncated and even in the case of synchronization the truncation effect may happen for some sinusoids.

In the case of application of some programs, removal of a part of samples or extension of measurement series by adding samples of zero values may be necessary. For instance the FFT program nested in Excel software demands sets of samples of size $N = 2^l$, where l - natural number.

In Fig.6 is shown the transform FM_{TZ} of the test set M_{TZ} obtained from the set M_T of $N = 480$ samples by complementing it with zeros up to $N = 512$ samples.

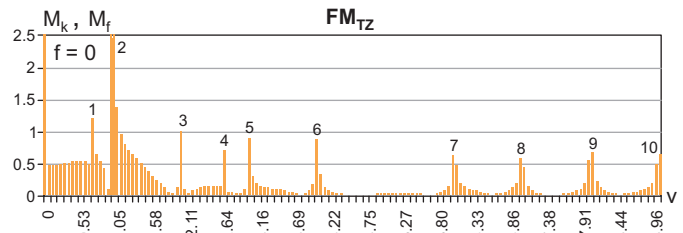


Fig. 6. The amplitude spectrum FM_{TZ} of the test run M_{TZ} formed by applying Excel software: M_{TZ} – test run obtained from the set M_T of $N = 480$ samples by complementing it with zeros up to $N = 512$ samples.

In the spectrum FM_{TZ} (Fig.6) the side stripes of significant values can be observed. The disturbances are analogous to those as in the case of truncation of the run (Fig.5).

The successive test run, M_{TR} , was obtained by adding, to the run M_T , pseudo-random disturbances of sampling frequencies generated by computer from the interval $\langle -5, 5 \rangle$ (of uniform distribution). As observed in Fig.7 the spectrum FM_{TR} contains a significant number of spectral disturbing lines.

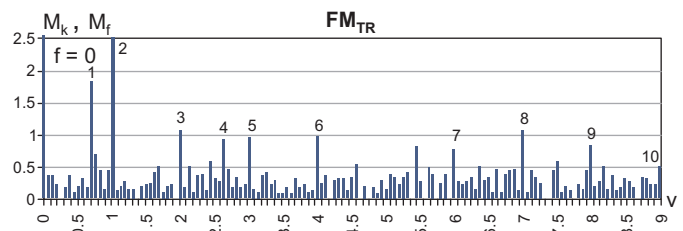


Fig. 7. The amplitude spectrum FM_{TR} of the test run M_{TR} formed by applying Matlab software: M_{TR} – test run obtained from the run M_T by adding pseudo-random disturbances from the interval $\langle -5, 5 \rangle$.

In the example shown in Fig.7 the spectral lines resulting from disturbances can be considered significant.

To prevent occurring such symptoms during measurements, as mentioned above, low-pass filters, synchronized recording and various time windows are applied [1, 2].

Approximation of runs by means of trigonometric polynomials and least-squares method (TLSA)

It should be stressed once more that any transform obtained by using the FFT contains complete measured information, i.e. together with disturbances of analyzed time series, hence this is time series transformation into domain of frequency and phase, performed in the way of interpolation of measurement data by means of trigonometric polynomials of a given uniform (natural) frequency scale.

Determination of spectral lines having their parameters close to real ones, which is connected with elimination of disturbances, can be realized by using the least-squares method, in the simplest case by assuming a power polynomial, as the orthogonal base, and sum of pairs of terms of a trigonometric polynomial :

$$y(t) = \sum_{u=0}^U c_u t^u + \sum_{k=1}^K (a_k \sin v_k t + b_k \cos v_k t) \quad (4)$$

$$t = 2\pi \frac{\tau}{T} ; \quad U + 2K < N$$

where :

- c_u – power polynomial coefficients
- a_k, b_k – trigonometric polynomial coefficients
- k – spectral line number
- t – angular axis, rad
- v_k – dimensionless spectral line frequency, $v_k > 0$
- τ – measurement axis (time, rotation angle, measurement point's number)
- T – period of main measurement axis
- U – number of power polynomial coefficients
- K – number of trigonometric polynomial coefficients
- N – size of set of measurement samples.

The power polynomial has been introduced to approximate the constant and trends. In the Matlab software linear trend of data can be removed by using the command „detrnd”. The trend is subtracted off the run by means of least-squares linear approximation. In the model (4) the power polynomial can be replaced by other functions τ , and varying frequency can be introduced, that may be reasonable in the case of analyzing some runs of specific models. However, level of computation outlays may be limiting in such case.

The coefficients c_u and a_k, b_k are determined from the condition for minimum of sum of squares of deviations, and this sum is used to assess approximation quality and extract significant spectral lines. Values of amplitudes and phases are determined by using the formulae (3). The model (4) differs from the interpolation formula (2) by that values of frequencies are not to be multiples of the fundamental period and total number of determined coefficients and spectral lines must be smaller than that of samples, N , to ensure some number of degrees of freedom necessary to make it possible to perform statistical significance assessment of determined coefficients and spectral lines.

The significant spectral lines are included one-by-one or collectively into the model with taking into account a degree of decreasing the sum of squares of deviations after their inclusion. If the successively included spectral lines do not make the sum of squares of deviations to decrease significantly then the approximation process will be stopped.

In this work to analyze the torque and angular speed runs (Fig.1) the least-squares approximation algorithm using

trigonometric polynomials (the TLSA method) in accordance with the author's elaboration based on the formulae (4) was applied.

However in this case the Nyquist's frequency limitation is also present. The problem is known in the approximation theory of discrete sets by using a set of selected functions where the functions are required not only to be mutually orthogonal in general, but also to be orthogonal on the approximated data set. It concerns arbitrary functions, also trigonometric ones.

The idea of the method of including - to approximation model - the function which most contributes to decreasing the sum of squares of deviations, is known in a general form, and as in the case of invention of the FFT it is connected with development and applications of computers [6]. Sometimes more firm results may be obtained by using the method of rejecting low-significant functions (terms). In such case the approximation is performed in successive steps with the use of a model which contains a redundant number of terms. Other strategies are also known [6]. In the considered examples of run analysis both approaches were applied. For relatively small sets of spectral lines (up to 50) a kind of algorithm and processing program applied to determining significant spectral lines is rather unimportant if confronted with vast computational capability of contemporary laptop computers.

Results of the determination of significant spectral lines in the spectrum of the measurement series M with the use of the least-squares approximation are presented in Tab.1.

Tab. 1. Results of the determination of significant spectral lines for the run M with the use of TLSA method : q – number of spectral line, v_q – frequency of spectral line, M_q – amplitude, Φ_q – phase, δ_q – degree of decrease of the sum of squares of deviations after including the spectral line q into the base of approximating functions .

q	1	2	3	4	5	6	7	8	9	10
v_q	1	0.7	2	3	4	8	9	6	7	2.6
M_q	10.46	1.66	1.03	1.04	1.01	0.99	0.92	0.87	0.82	0.80
Φ_q	0.86	0.66	0.97	-1.31	1.76	-1.33	-0.01	1.22	-0.34	-1.48
δ_q [%]	83.7	13.3	5.8	6.1	6.4	6.5	5.9	5.8	5.4	5.4
q	11	12	13	14	15	16	17	18	19	
v_q	15	2.3	1.3	5	13	14	11	12	10	
M_q	0.89	0.54	0.42	0.40	0.41	0.36	0.31	0.22	0.21	
Φ_q	1.57	1.35	-1.43	1.33	-0.76	0.97	1.25	-0.63	-1.19	
δ_q [%]	5.9	2.4	1.5	1.4	1.4	1.1	0.8	0.4	0.4	

In the above presented example the searching for significant spectral lines was realized by hand without using the FFT in advance. The values v given in Tab.1 were rounded to one digit after the point. Some of them were determined with a greater accuracy (up to 3 significant digits). Sequence of including the spectral lines is of no influence on final result of approximation and precise positioning the spectral lines regarding their share in decreasing the minimum of sum of squares of deviations is not performed in practice but some influence levels are assumed instead, which makes the process of searching for spectral lines much faster and its automation possible.

On the basis of the constant and first 10 spectral lines, was built the test run M_1 (Fig.2) which constitutes the least-squares approximation of the run M containing the constant and strictly the first 10 amplitude spectral lines (Fig.2) and 10 respective phases.

To check the method of searching for significant spectral lines the test runs M_T , M_{TD} and M_{TR} were analyzed also by using the TLSA method together with an algorithm for including and excluding the spectral lines (Tab.2).

Tab. 2. Results of the determination of main spectral lines in spectra of the test runs with the use of TLSA method : QM_T – spectrum of the run M_T , QM_{TD} – spectrum of the run M_{TD} , QM_{TR} – spectrum of the run M_{TR} .

	q	1	2	3	4	5	6	7	8	9	10
QM_T	v_q	1	0.7	2	3	4	8	9	6	7	2.6
	δ_q [%]	91.7	28.4	15.1	17.5	20.8	25.0	28.6	36.6	51.4	100
QM_{TD}	v_q	1	0.7	2	3	4	8	9	6	7	2.6
	δ_q [%]	91.5	27.5	14.9	17.0	20.6	24.6	29.0	37.0	51.2	100
QM_{TR}	v_q	1	0.7	2	3	4	8	9	6	7	2.7
	δ_q [%]	80.1	15.0	4.6	3.4	4.4	3.4	1.2	3.0	5.8	4.6

From Tab.2 it results that among the first 10 spectral lines for each of the analyzed runs the spectral lines of the same frequencies can be found. The obtained result of 100% decrease of the sum of squares for 10th spectral line in the spectra QM_T and QM_{TD} is obvious in this case.

Also, in the case of the run M_{TR} (Tab.2) within the set of significant spectral lines 10 of them have the same frequencies, that confirms effectiveness of the method. The level of disturbances introduced into the run M_{TR} was significant as the maximum amplitudes of the disturbances reached 30% of the maximum values of amplitudes of the run M_T .

The absence of correct order of some spectral lines, observed in Tab.2, as regards the decreasing of the sum of squares of deviations is not a mistake but manifestation of features of orthogonalization process after inclusion of successive spectral lines. The analogous result is obtained in every attempt to changing this sequence of the spectral lines. Such phenomena can happen when values of amplitudes of spectral lines are close to each other and their share in approximation of run is similar and concerns groups of a few spectral lines (2 or 3) that makes determining the spectral lines only a little more difficult.

SYNCHRONOUS AVERAGING AND MOVABLE APPROXIMATION OF RUNS

Run synchronous averaging

Sampling the torque run M was timed by pulses from shaft angle position and for successive rotations of the shaft the angular positions of sampling points could be assumed identical. For each of the shaft rotations 30 measurements initiated by shaft angular position, were made.

Therefore for steady loading conditions of propulsion system the measurements performed within a given shaft rotation constitute successive realizations of the same process and the deviations from mean values in successive points can be considered random ones which have the sum of deviations from the mean tending to zero along with increasing number of samples. Hence it is reasonable to perform the synchronous averaging of run (called also : coherent, linear, prior-detecting or vectorial averaging) [2]. It should be mentioned that the averaging is a point-wise least-squares approximation procedure.

Fig.8 shows which way the differences between the measured run and its averaged values go depending on a number of synchronous averaging cycles.

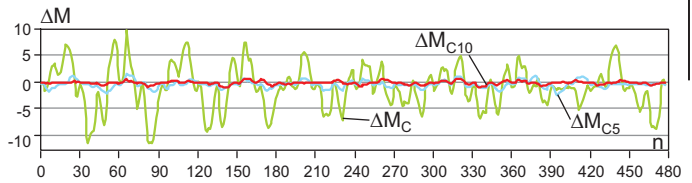


Fig. 8. Runs of the cyclic differences $\Delta M = \Delta M_{(n+30)} - \Delta M_n$ for some selected numbers of synchronous averaging cycles : ΔM_{C1} – without averaging, ΔM_{C5} – for 5-cycle averaging, ΔM_{C10} – for 10-cycle averaging.

The runs ΔM for the whole range of n were achieved by extending the run M by the successive run M . To assess effectiveness of the averaging procedure also the runs of Pearson's correlation coefficient values synchronically calculated can be applied (Fig.9).

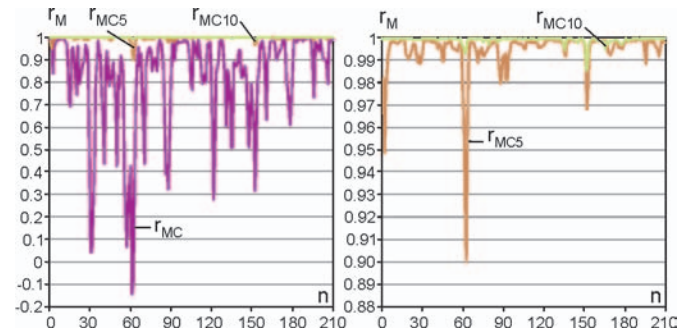


Fig. 9. Runs of the Pearson's correlation coefficient r_M determined for the neighbouring cycles of the run M_M : r_{MC} – without averaging, r_{MC5} – for averaging after 5 cycles, r_{MC10} – for averaging after 10 cycles.

The runs ΔM are characterized by the deviations between the points distant by one cycle, but the runs r_M are characterized by their trends. To determine r_M values for each of them 5 successive samples were taken into consideration.

In the case of the analyzed data set the maximum possible number of averaging was 16. In Fig.10 a fragment of the measured run M and the averaged run M_{C16} (for 16-cycle averaging) is compared, as well as the run of the standard deviations S_M is presented.

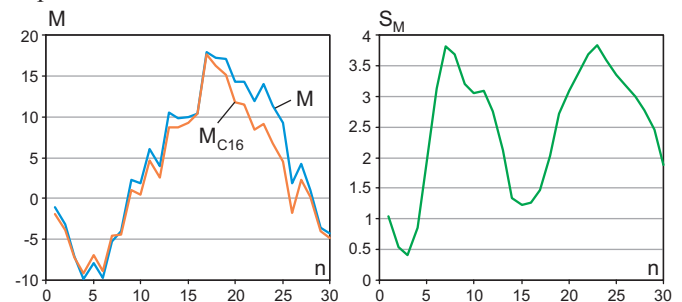


Fig. 10. Comparison of a fragment of the measured run M and the averaged run M_{C16} (for 16-cycle averaging): S_M – standard deviation of the run M .

It is easy to observe that the waving period of the standard deviations S_M (Fig.10) amounts to about 0.7 of the shaft rotation period, hence it can be concluded that this is the large amplitude of torsional vibrations of the propulsion system (i.e that fitted with one-cylinder combustion engine) which constitutes the main cause of torque measurement disturbances. The smoothness disturbances observed in the run M_{C16} may result from manufacturing and assembling inaccuracies of the discs.

The FFT of the single averaged run obtained contains spectral lines solely for integral values of v (Fig.11).

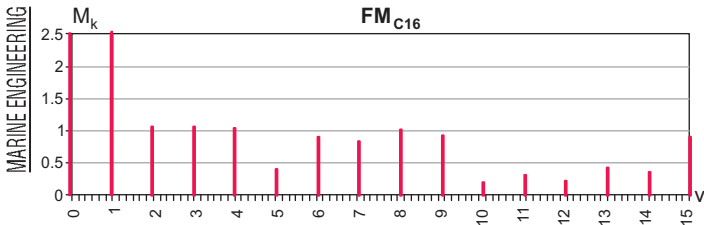


Fig. 11. The amplitude spectrum FM_{C16} of the run M_{C16} , obtained with the use of Matlab software.

In Fig.12 a fragment of the averaged run M_{C16} was compared with its two trigonometric approximations for an assumed number of spectral lines, obtained by means of the least squares method.

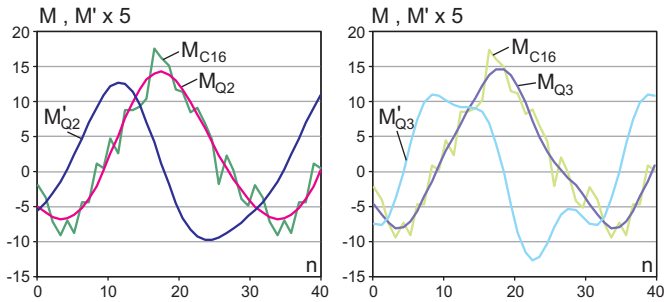


Fig. 12. Comparison of the averaged run M_{C16} and its approximations: M_{Q2} – that based on the spectral lines $q = 1, 2$; M_{Q3} – that based on the spectral lines $q = 1, 2, 3$ (Tab.4); M'_{Q2} , M'_{Q3} – their first derivatives.

In order to better demonstrate differences between the runs M_{Q2} and M_{Q3} the runs of their first derivatives M'_{Q2} and M'_{Q3} are also presented (Fig.12). However in both the cases shown in Fig.12 one may doubt, making only the use of general knowledge on physical nature of the run M , whether the approximation models are correct. Possible adding successive spectral lines would decrease quality of the approximation. It will be further demonstrated that the problem of smoothing the run does not consists in adding or removing the spectral lines which appeared in the spectrum of the run M .

The information removed from the run M as a result of averaging has been now stored in the run of deviations, ΔM_{C16} whose FFT obtained by means of the Matlab, is shown in Fig.13.

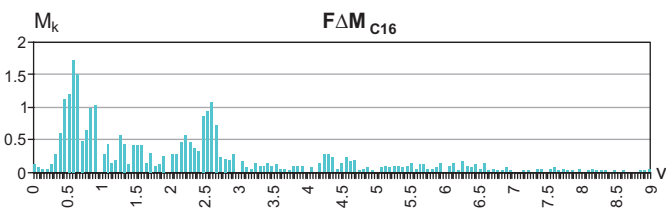


Fig. 13. A fragment of the amplitude spectrum $F\Delta M_{C16}$ obtained by means of the Matlab for the run of deviations, $\Delta M_{C16} = M - M_{C16}$.

In Tab.3 are presented results of searching for the most significant spectral lines in the run ΔM_{C16} , by using the least squares method.

Tab. 3. Results of determining the most significant spectral lines for the run of deviations, ΔM_{C16} , by using the TLSA method.

q	1	2	3	4	5	6	7	8	9	10
v_q	1	0.6	0.7	0.5	0.9	2.6	2.3	1.3	1.4	2.8
δ_q [%]	0.0...	24.4	30.1	9.7	5.7	10.8	5.8	4.1	2.8	2.7
ΔM_{C16q}	0.11	1.77	1.69	0.81	0.6	0.81	0.53	0.44	0.35	0.34

In Tab.3 the spectral line of $v_1 = 1$ was left in order to demonstrate effectiveness of the performed averaging. The value of the spectral line amplitude $\Delta M_1 = 0.17$ appeared significantly smaller as compared with that of the averaged run $M_2 = 10.46$ (Fig.2, that confirms good effectiveness of the performed averaging.

In addition, the spectrum $Q\Delta M_{C16}$ is graphically presented (Fig.14) to facilitate making comparisons with the spectrum $F\Delta M_{C16}$ (Fig.13).

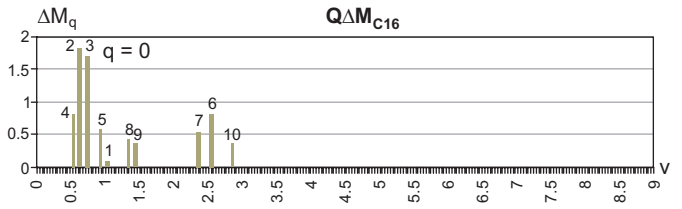


Fig. 14. Main spectral lines of the amplitude spectrum $Q\Delta M_{C16}$ obtained by using the TLSA method for the run of deviations, $\Delta M_{C16} = M - M_{C16}$.

The run of deviations, ΔM_{C16} , and runs of its selected approximations are shown in Fig.15.

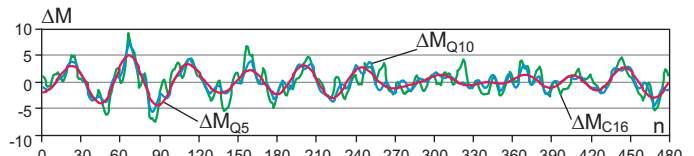


Fig. 15. The run of deviations, $\Delta M_{C16} = M - M_{C16}$, and its selected LSA approximations: ΔM_{Q5} – that containing the spectral lines for $q = 2 - 5$, ΔM_{Q10} – that containing all 10 spectral lines (Fig.14).

From the comparison of the runs shown in Fig.15 it results that four neighbouring spectral lines of $k = 2-5$ are mainly responsible for the observed „beating” (Fig.14).

The run of deviations, ΔM_{C16} , can be also subjected to further synchronous averaging for selected non-integral frequencies v and such operation can be repeated in order to split the disturbances regarding their characteristic frequencies – in an analogous way as it takes place in the case of approximation itself.

Examples of synchronous averaging the run of deviations, ΔM_{C16} , for two values of v are shown in Fig.16.

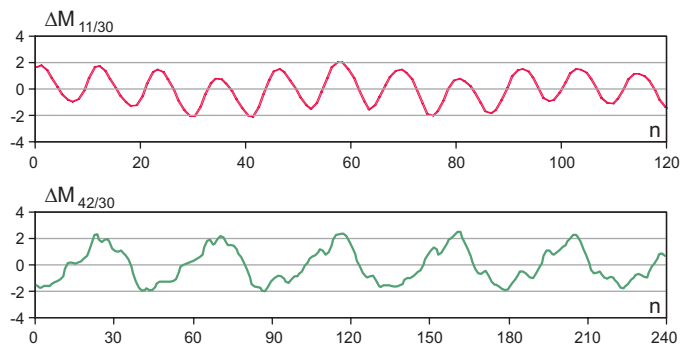


Fig. 16. Results of synchronous averaging of the run of deviations, ΔM_{C16} , of 10 averaging operations, for the various values of v : $M_{11/30}$ – a fragment of the averaged run for $v = 11/30$, $M_{42/30}$ – a fragment of the averaged run for $v = 42/30$.

The above mentioned procedures could be applied again to the obtained runs or those of differences resulting from the averaging in order to finally extract interesting periodic components. Limited accuracy of v - values make a problem in their setting. In the case of the run in question they arise from the number of samples derived from one shaft revolution.

The synchronous averaging method should be considered as basic one for processing the data of periodical character, measured in steady operation conditions of propulsion system.

Smoothing the runs by means of movable approximation method

In the systems for measuring torque or angular speed the main aim of the processing of measurement results is to determine in real time the runs of the quantities, characterized by an appropriately low level of disturbances. Examples of smoothing the run M_{C16} with the use of two different approximating objects elaborated by this author [9], are shown in Fig.17.

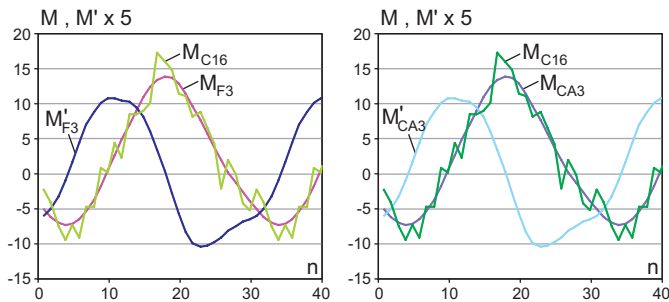


Fig. 17. Comparison of the averaged torque run M_{C16} and its approximations obtained by using the movable approximation method: M_{F3} – the result of the triple approximation by using 3rd order power polynomial (Savitzky's – Golay's filter) within the interval of 11 samples; M_{CA3} – the result of the triple approximation by using 3rd order power polynomial within the interval of 21 samples and 2 nodes having free constraints (cut derivatives: 1st; 2nd and 3rd); M'_{F3} , M'_{CA3} – 1st derivatives.

As results from the comparison of the runs M_{F3} and M_{CA3} as well as their derivatives M'_{F3} and M'_{CA3} , the achieved results are identical in the applied scale of imaging. The differences are negligible and they can be disclosed e.g. by comparing the higher order derivatives or remote significant places of values of spectral lines of Fourier transforms. As already mentioned there is a justified supposition that the approximations by using trigonometric polynomials (Fig.12) are loaded by large errors resulting from a trigonometric model inadequacy, that can be concluded from the comparison of the runs of 1st derivatives for both the approximation cases (Fig.12 and 17). The problem can be solved by analyzing the motion models of propulsion system, e.g. by taking into consideration a run of indicated pressure.

If the Fourier transform for the runs M_{F3} and M_{CA3} (Fig.17) is elaborated it will have the form shown in Fig.18, whereas the FFT of the run M_{O2} consists 2 spectral lines, and that of the run M_{O3} - 3 ones (plus constant) taken from the transform FM_{C16} (Fig.11).

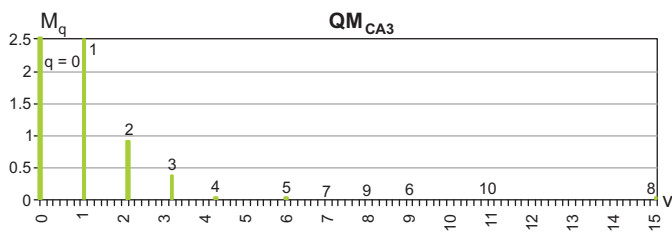


Fig. 18. Ten main spectral lines of the amplitude spectrum QM_{CA3} , determined by using the least squares method for the smoothed run M_{CA3} .

The transform QM_{CA3} (Fig.18) is characteristic by having a dozen or so spectral lines of similarly small values of amplitudes but significantly important for approximation quality (smoothing) of the run, which is manifested by a large degree of decreasing the sum of squares of deviations after adding successive spectral lines (Tab.4).

Tab. 4. Values of input data to determination process of main spectral lines and their parameters for the spectrum QM_{CA3} (Fig. 18).

q	1	2	3	4	5	6	7	8	9	10
v_q	1	2	3	4	6	9	7	15	8	11
δ_q [%]	99.3	84.6	98.9	71.9	83.3	56.1	77.2	94.2	70.7	54.0
M_{CA3q}	10.23	0.82	0.34	0.031	0.018	0.006	0.005	0.002	0.0005	0.0002

In order to fully recognize differences between the runs their phase spectra should be also compared. In Fig.19 is shown the run of the deviations, ΔM_{CA3} , between the run ΔM_{C16} and the smoothed run M_{CA3} .

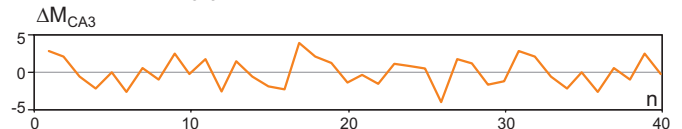


Fig. 19. The run of deviations: $\Delta M_{CA3} = M_{C16} - M_{CA3}$

The transform of the above mentioned deviations amounts approximately to the difference of the spectrum FM_{C16} (Fig.11) and QM_{CA3} (Fig.18).

Smoothing by means of the movable approximation method can be also applied to the runs of deviations ΔM_{C16} .

Smoothing by means of the movable approximation method and decomposition of disturbances can be applied both before and after synchronous averaging. A very important advantage of the movable approximation is its possible application to smoothing and decomposing the disturbances measured in unsteady conditions: starting-up, stopping, variable loading. The disturbances extracted as a result of decomposition can be next subjected to frequency analysis, if necessary.

Alternative smoothing the runs by applying the Fourier inverse transform would require prior multiplication of the transforms by appropriate weighting functions. In order to find such weighting functions it would be necessary to smooth the runs in advance e.g. by applying the movable approximation.

Interim averaging per cycle

The interim averaging per cycle is a peculiar case of the movable approximation. It is aimed at imaging the variability of mean values usually determined as a function of time or shaft rotation angle. Such characteristics may be important for diagnostics of propulsion systems. In Fig.20 are presented results of interim averaging the runs of torque and angular speed oscillations, shown in Fig.1.

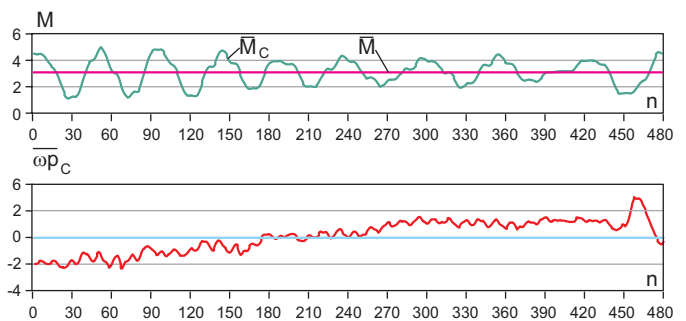


Fig. 20. Results of interim averaging the runs M and ω_p (Fig. 1): \overline{M}_c , $\overline{\omega_p}_c$ – results of averaging per one cycle (rotation), \overline{M} – mean value of the set.

The achieved results can be used in successive steps of their analyzing with the use of the above presented methods of data processing.

CONCLUSIONS

- The methods of synchronous averaging and movable approximation should be deemed basic for processing the discretely measured runs of torque and angular speed.
- The spectral analysis with the use of least-squares approximation of random disturbances and uneven sampling makes it possible to extract significant spectral lines in the situation of truncated run, random disturbances and non-uniform sampling. It also makes it possible to precisely determine characteristic frequencies as well as extract significant spectral lines of neighbouring frequencies.
- The FFT can be used for preliminary recognizing the spectrum if there is no computer program available for automatic determining the significant spectral lines by means of least-squares approximation.

NOMENCLATURE

- a_k, b_k – trigonometric polynomial coefficients
 a_0 – trigonometric polynomial constant
 c_u – power polynomial coefficients
 $F...$ – Fourier transform of a given run
 k – spectral line number
 K – number of trigonometric polynomial coefficients
 M – torque, measured torque
 M_{C16} – torque run synchronically averaged per 16 cycles
 M_T – torque test run containing 10 spectral lines
 M_{TD} – test run obtained from the run M_T by removing 10 samples from each end of set of samples
 M_{TR} – test run obtained from the run M_T by adding to it random disturbances from the interval $\langle -5, 5 \rangle$
 M_{TZ} – test run obtained from the run M_T by its extending by zeros as to reach $N = 512$ samples
 n – number of a sample in measurement set : 1, ..., N
 N – number of samples in measurement set
 $Q...$ – spectrum of a given run, obtained by using LSA method
 t – angular axis, rad
 T – period
 U – number of power polynomial coefficients
 ΔM – run of deviations of the run M (a kind of deviations is indicated by its indices)
 ΔM_{C16} – run of deviations, $\Delta M_{C16} = M - M_{C16}$
 δ_q – degree of decreasing the sum of squares of deviations after including the component q to the basis of approximating functions
 v – frequency
 v_k – dimensionless spectral line frequency, $v_k > 0$
 τ – time
 Φ – phase.

Indices

- f – number of a distinguished (significant) component of a spectrum (spectral line) in Fourier transform
 g – limit value
 k – successive number of spectral line in Fourier transform
 q – number of spectral line in the transform obtained by means of TLSA method
 $'$ – symbol of 1st derivative.

Abbreviations

- DFT – Discrete Fourier Transform
 FFT – Fast Fourier Transform
 TLSA – approximation by means of trigonometric polynomials and least squares method.

BIBLIOGRAPHY

1. Lynos R. G.: *Introduction to the digital processing of signals* (in Polish), WKŁ (Communication publishing house), Warszawa, 2003

2. Max J.: *Mietydy i technika obrabotki signalow pri fizycznych zmierienijach* (translation from French, 1981), v.1, MIR, Moskwa, 1983
3. Morawski L., Polanowski S., Szuca Z.: *Processing stand-test results of a photo-optic torque meter with the use of movable approximation* (in Polish). Proc. of 26th Symp. on Ship Power Plants. Zeszyty Naukowe AMW (Scientific Bulletins of Polish Naval Academy). 2005
4. Morawski L., Sikora M.: *Application of the photo-optic torque meter to estimation of torque and rotational speed fluctuations of the propeller shaft of ship*. 6th Slovak and Czech Conference : SENSOR and SENSOR SYSTEM '97. Kosice-Presov. 1997
5. Polanowski. S.: *The processing of indicator diagrams with the use of the moving approximating objects*. Combustion Engines. No 1/2005
6. Enslein K., Ralston A., Wilf H. S. (Editors): *Statistical Methods for Digital Computers*. J. Wiley, 1977

CONTACT WITH THE AUTHOR

Stanisław Polanowski, D.Sc., Eng.
 Mechanic-Electric Faculty,
 Polish Naval University
 Śmidowicza 69
 81-103 Gdynia, POLAND
 e-mail : SPolanowski@o2.pl

Conference

REGIONAL GROUP of the Section on Exploitation Foundations

On 23 March 2006 Faculty of Ocean Engineering and Ship Technology, Gdańsk University of Technology, hosted the members of the Regional Group of the Section on Exploitation Foundations, Machine Building Committee, Polish Academy of Sciences (PAS), who took part in their successive scientific seminar.

The seminar's scientific program consisted of four papers presented by the scientific workers of the Faculty :

- *Comparative analysis of main engine loads and output of multi-bucket dredgers by using probabilistic approach* – by D. Bocheński
- *Diagnostics of the energy transformation process of steam turbine power plant of large output* – by J. Gluch
- *Research on water-lubricated short-sleeve bearings of propeller shaft* – by W. Litwin
- *A concept of application of artificial neural networks to represent reliability probabilistic models* – by J. Rudnicki

After interesting discussion on the presented topics the seminar participants were acquainted with the Faculty's scientific and didactic laboratories.

Calculation of the mean long-term service speed of transport ship

Part I

Resistance of ship sailing on regular shipping route in real weather conditions

Tadeusz Szelangiewicz

Katarzyna Żelazny

Szczecin University of Technology

ABSTRACT

Service speed obtainable by a ship in real weather conditions when sailing on a given shipping route, is one of the major parameters which have great impact on ship operation costs. The so far used, very approximate method of service speed prediction based on "service margin", is very little exact. In this paper a new method based on additional ship resistance dependent on mean statistical parameters of wave and wind occurring on a given shipping route, is presented. The mean long-term service speed is calculated on the basis of the calculated additional resistance and the screw propeller and propulsion engine parameters. Also, a new definition of service margin and a way of its calculation is presented apart from the results of the mean service speed calculation depending on ship's type and size and shipping route.

Keywords : ship service speed, wind, waving, shipping route, service margin, long-term prediction.

INTRODUCTION

The ship owner, when planning building a new ship, on the basis of his experience and knowledge of shipping market, determines the ship's deadweight and predicts its service speed to be reached by the ship on a given shipping route. The service speed obtainable by a ship in real weather conditions (mainly wind and waves) is one of the most important parameters greatly influencing ship's profitability on a given shipping route. In the design algorithms used today in ship design offices, ship's deadweight is determined with a satisfactory exactness, but calculation of ship's service speed is rather inexact and practically known already after ship's delivery and some time of its service. Hence in the ship building contract, is given another speed, so called contract speed which the ship has to achieve in still-water conditions. On the basis of still-water resistance characteristics and rated output of propulsion engine, the obtainable ship service speed is predicted by accounting for relevant coefficients, Fig.1.

In that prediction an increase of ship resistance in service conditions in relation to that in still water conditions (represented by the service margin SM in Fig.1) is not exactly determined as it depends on real weather conditions occurring on a given shipping route.

Basing on known statistical data on winds and waves possible to occur on a given shipping route, one is capable in determining a long-term distribution function of additional resistance, and next, for an assumed main engine output, a long-term distribution function of ship's speed possible to

be obtained on a given shipping route. Such approach makes it possible not only to exactly determine the mean statistical service speed of the ship, but also to investigate the influence of power output of a selected main engine on the ship's service parameters including its long-term service costs.

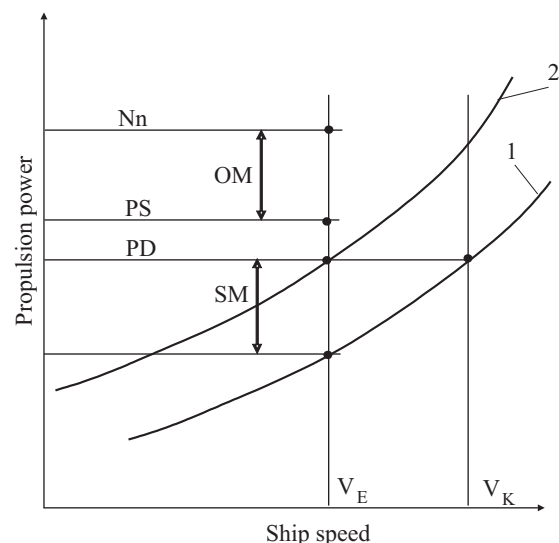


Fig. 1. Predicted service speed of a ship. **Notation :** N_n – rated output of engine, PS – shaft power; PD – power at propeller's cone, OM – operational margin, SM – sea margin, V_K – contract speed, V_E – predicted service speed, 1 – propeller curve for still-water conditions, for non-fouled hull, 2 – predicted propeller curve with service margin, for real conditions .

Attempts to determine the service speed of ship in real weather conditions have been already reported in [4, 23, 24], however there were not accounted for statistical distributions of wind and wave parameters met on a given shipping route.

STATISTICAL LONG-TERM PARAMETERS OF WINDS AND WAVES ON SHIPPING ROUTES

In order to determine the mean long-term ship service speed the ship's resistance in real weather conditions should be determined in advance. The statistical long-term wave parameters, namely : H_s - the significant wave height, T_1 - the mean characteristic period, μ - the mean geographical direc-

tion, were determined on the basis of multi-year measurements. Results of the measurements are contained in the atlas of wave parameters [10] and in extended form in [11], in which seas and oceans have been divided additionally into the set of sea areas shown in Fig.2 (where each sea area is characterized by its own statistical wave parameters).

The atlases [10] and [11] contain sample size of waves characterized by H_s and T_1 parameters and recorded in a given area for a given season and wave direction μ , as exemplified in Tab.1. On the basis of these data, was elaborated a computer database on the waves met on seas and oceans, which contains the occurrence probabilities of waves with H_s , T_1 parameters, f_{HT} , and the occurrence probabilities of μ directions, f_μ , for all the sea areas (split into seasonal data), as exemplified in Tab.2 and 3.

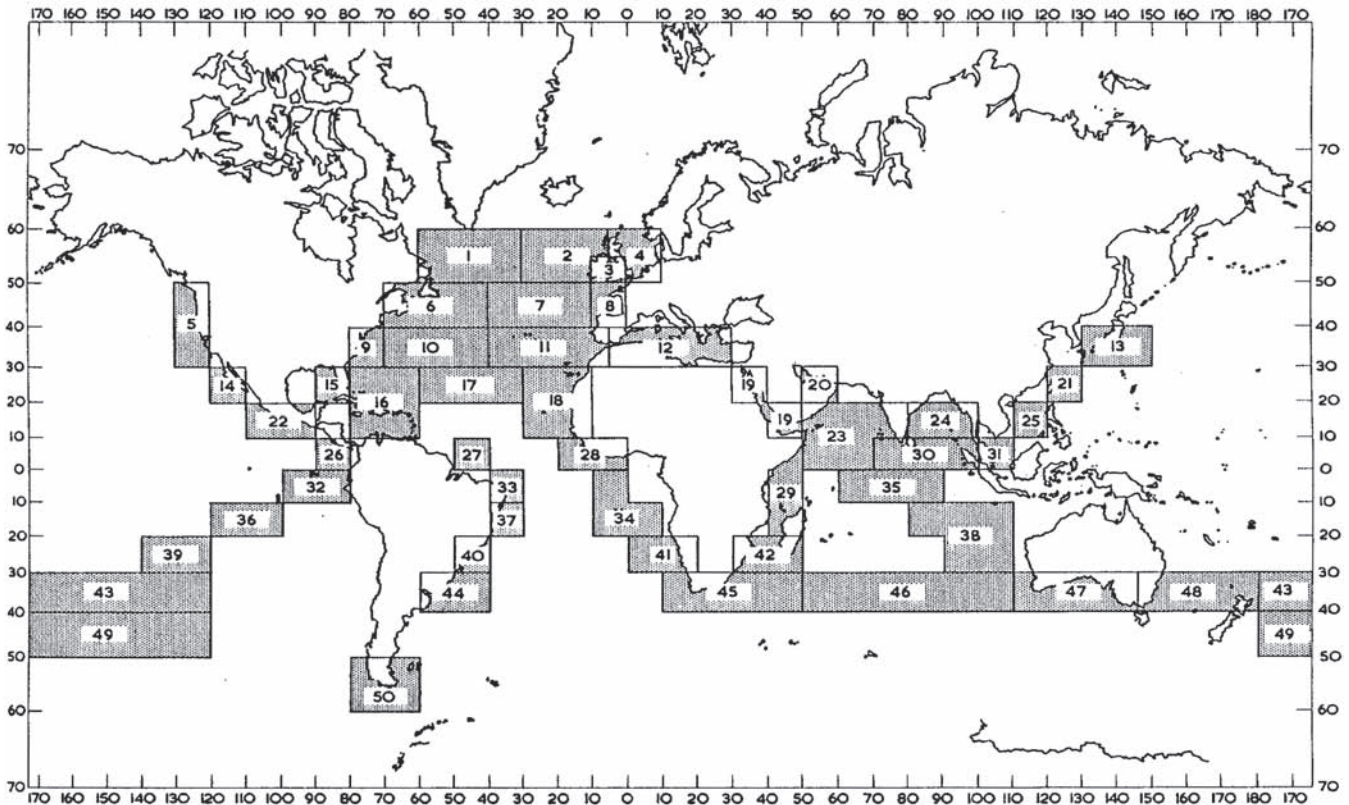


Fig. 2. Oceans divided into set of sea areas, acc. [10] .

Tab. 1. Sample size of waves of H_s height and T_1 period for a given μ direction and sea area [10] .

Sea area : 1											
Season of the year : December – February (winter)											
Wave direction : $\mu = 000$ deg											
H_s [m] \ T_1 [s]	calm	< 5	6 ÷ 7	8 ÷ 9	10 ÷ 11	12 ÷ 13	14 ÷ 15	16 ÷ 17	18 ÷ 19	20 ÷ 21	> 21
0.25		2									
0.5		1	1	1							
1.0		8	2	1	1						
1.5		2	4	5		2					
2.0			5		3						
2.5		1	5	4	3						
3.0			1	3	2	1					
3.5			1	4	5						
4.0				1	1	4	1	1			
4.5				4	2		1	1			
5.0					1						
6.0				1							
6.5				1	2						
7.5					1						

Tab. 2. The occurrence probabilities, f_{HT} , of wave of H_s height and T_1 period for a given μ direction and sea area [10].

Sea area : 1											
Season of the year : December – February (winter)											
Wave direction : $\mu = 000$ deg											
H_s [m] \ T_1 [s]	calm	< 5	6 ÷ 7	8 ÷ 9	10 ÷ 11	12 ÷ 13	14 ÷ 15	16 ÷ 17	18 ÷ 19	20 ÷ 21	> 21
0.25		0.023									
0.5		0.011	0.011	0.011							
1.0		0.091	0.023	0.011	0.011						
1.5		0.023	0.045	0.057		0.023					
2.0			0.057		0.034						
2.5		0.011	0.057	0.045	0.034						
3.0			0.011	0.034	0.023	0.011					
3.5			0.011	0.045	0.057						
4.0				0.011	0.011	0.045	0.011	0.011			
4.5				0.045	0.023		0.011	0.011			
5.0					0.011						
6.0				0.011							
6.5				0.011	0.023						
7.5					0.011						

Tab. 3. The combined probability, $f_{HT} \cdot f_{\mu}$, of occurrence of wave of H_s height and T_1 period, with taking into account the probability f_{μ} for each direction μ in a given sea area, [10].

Sea area: 1											
Season of the year : December – February (winter)											
Wave direction : all											
H_s [m] \ T_1 [s]	calm	< 5	6 ÷ 7	8 ÷ 9	10 ÷ 11	12 ÷ 13	14 ÷ 15	16 ÷ 17	18 ÷ 19	20 ÷ 21	> 21
0.25	0.0021	0.0064	0.0009								
0.5	0.0004	0.0137	0.0026	0.0013							0.0017
1.0	0.0043	0.0321	0.0160	0.0026	0.0026	0.0013					0.0004
1.5	0.0064	0.0180	0.0570	0.0206	0.0038	0.0026					0.0009
2.0	0.0086	0.0073	0.0450	0.0364	0.0193	0.0051	0.0017	0.0004	0.0004		
2.5	0.0073	0.0056	0.0385	0.0501	0.0308	0.0069	0.0030	0.0009	0.0004		
3.0	0.0137	0.0009	0.0175	0.0377	0.0287	0.0112	0.0017	0.0004	0.0004		
3.5	0.0060	0.0009	0.0124	0.0334	0.0347	0.0167	0.0043	0.0013			
4.0	0.0060	0.0017	0.0043	0.0248	0.0180	0.0116	0.0034	0.0009			
4.5	0.0043	0.0009	0.0051	0.0257	0.0218	0.0111	0.0060	0.0051			0.0004
5.0	0.0017		0.0013	0.0013	0.0030	0.0026		0.0009			
5.5	0.0004		0.0021	0.0017	0.0043	0.0039	0.0021	0.0009			
6.0	0.0004	0.0009	0.0026	0.0094	0.0099	0.0034	0.0030	0.0013			
6.5	0.0009		0.0034	0.0094	0.0081	0.0069	0.0039				
7.0	0.0004			0.0009	0.0051	0.0017	0.0009		0.0004		
7.5	0.0017		0.0004	0.0017	0.0073	0.0064	0.0013	0.0004			0.0004
8.0	0.0013	0.0004	0.0009	0.0009	0.0056	0.0030	0.0004	0.0009			
8.5			0.0004	0.0013	0.0038	0.0017	0.0004	0.0004			
9.0			0.0004	0.0013	0.0034	0.0004	0.0004		0.0004		
9.5	0.0009			0.0026	0.0026	0.0034	0.0009	0.0013	0.0021		0.0004
15					0.0004						

The statistical wave parameters used for calculation of ship resistance due to wind and waves should be correlated with the wind parameters: V_A - mean wind speed, γ_A - mean statistical geographical direction of wind. As such atlases for wind do not exist the appropriate relations between wind and wave parameters were elaborated on the basis of measurements [3, 25].

Basing on literature sources, one elaborated the relations $V_A = V_A(H_s, T_1)$ for the purposes of this work, assuming that:

- ✦ Wind direction coincides with wave direction :

$$\gamma_A = \mu^* \quad (1)$$

- ✦ The occurrence probability of wind direction, f_{γ_A} , is the same as that of wave direction, f_{μ} :

$$f_{\gamma_A} = f_{\mu} \quad (2)$$

- ✦ The occurrence probability of mean wind speed, f_{V_A} , is the same as that of wave of H_s, T_1 parameters, f_{HT} :

$$f_{V_A} = f_{HT} \quad (3)$$

Results of calculations of the relations $V_A = V_A(H_s, T_1)$ for the wave parameters contained in [10], were published in [25].

* in the literature on wind-generated sea waves it is assumed that if the difference between wind and wave directions does not exceed 30° then both the directions are the same; such state occurs during 80% time of observations on seas and oceans [6, 22]

SHIP RESISTANCE IN REAL WEATHER CONDITIONS

In real weather conditions during sea voyage of a ship on a given shipping route, its total resistance consists of still-water resistance and additional components :

$$R_C = R + \Delta R \quad (4)$$

where :

R – still-water resistance of ship (accounting for the drift angle and possible surface sea current)

ΔR – additional ship resistance resulting from real sailing conditions :

$$\Delta R = R_{xA} + R_{xW} + R_{xR} \quad (5)$$

R_{xA} – additional wind-generated resistance

R_{xW} – additional wave-generated resistance

R_{xR} – additional resistance resulting from e.g. rudder action to keep a given ship course.

STILL-WATER RESISTANCE OF SHIP

The ship's still-water resistance is usually measured (by model testing) or calculated for the ship in rectilinear motion. In real weather conditions the ship sails under a certain drift angle due to oblique action of wind and waves or/and possible surface sea current. Hence the still-water response for the ship at steady speed, is composed of :

$$\begin{aligned} R_x &= \frac{1}{2} \rho S V_{RV}^2 C_x(\beta_{RV}) \\ R_y &= \frac{1}{2} \rho S V_{RV}^2 C_y(\beta_{RV}) \\ M_z &= \frac{1}{2} \rho S L V_{RV}^2 C_m(\beta_{RV}) \end{aligned} \quad (6)$$

where :

R_x, R_y, M_z – components of still-water resistance forces and moment of ship sailing at drift angle β_{RV} , and surface sea current, respectively, (Fig.3)

ρ – water density

S – lateral projection of underwater ship hull surface onto ship's plane of symmetry (PS)

V_{RV} – relative ship speed

β_{RV} – relative drift angle

L – ship length

C_x, C_y, C_m – coefficients of resistance forces and moment.

In Eqs. (6) the relative speed and relative drift angle is as follows :

$$V_{RV} = \sqrt{V_{RVx}^2 + V_{RVy}^2} \quad (7)$$

$$\beta_{RV} = \arctg \frac{-V_{RVy}}{V_{RVx}} \quad (8)$$

$$\left. \begin{aligned} V_{RVx} &= V_x - V_C \cos \beta_C \\ V_{RVy} &= V_y - V_C \sin \beta_C \end{aligned} \right\} \quad (9)$$

where :

V – absolute ship speed

$V_x = V \cos \beta$ } – absolute ship speed

$V_y = -V \sin \beta$ } components

β – drift angle at absolute speed

V_C – surface sea current velocity

β_C – sea current direction relative to ship

$$\beta_C = \gamma_C - \psi \quad (10)$$

γ_C – geographical direction of surface sea current, ($\gamma_C = 0^\circ$ northbound current, $\gamma_C = 90^\circ$ eastbound current)

ψ – geographical course of ship, ($\psi = 0^\circ$ northward course, $\psi = 90^\circ$ eastward course).

If the sea current velocity $V_C = 0$ then the absolute ship speed V and absolute drift angle β is valid for Eqs. (6).

In the subject-matter literature can be found various empirical formulae based on the tests of many ship models, by means of which values of the coefficients $C_x, C_y, C_m(\beta_{RV})$ can be calculated. In [20], the coefficients C_x, C_y, C_m for the directions defined in Fig.3, have the following form :

$$\begin{aligned} C_x &= 0.075 \sin \left[\left(180^\circ - \arcsin \frac{C_{x_0}}{0.075} \right) \left(1 - \frac{\beta_{RV}}{k_x} \right) \right] \\ C_y &= 0.5 C_1 \sin 2\beta_{RV} \cos \beta_{RV} + \\ &+ C_2 \sin^2 \beta_{RV} + C_3 \sin^4 2\beta_{RV} \end{aligned} \quad (11)$$

$$\begin{aligned} C_m &= m_1 \sin 2\beta_{RV} + m_2 \sin \beta_{RV} + \\ &+ m_3 \sin^3 2\beta_{RV} + m_4 \sin^4 2\beta_{RV} \end{aligned}$$

where :

$C_{x_0}, k_x, C_1, C_2, C_3, m_1, m_2, m_3, m_4$ – the coefficients dependent on ship hull parameters, and $S = L \cdot T \cdot \sigma$ (where : T – ship draught, σ – reduction factor for underwater hull surface side area) is the surface used in this method.

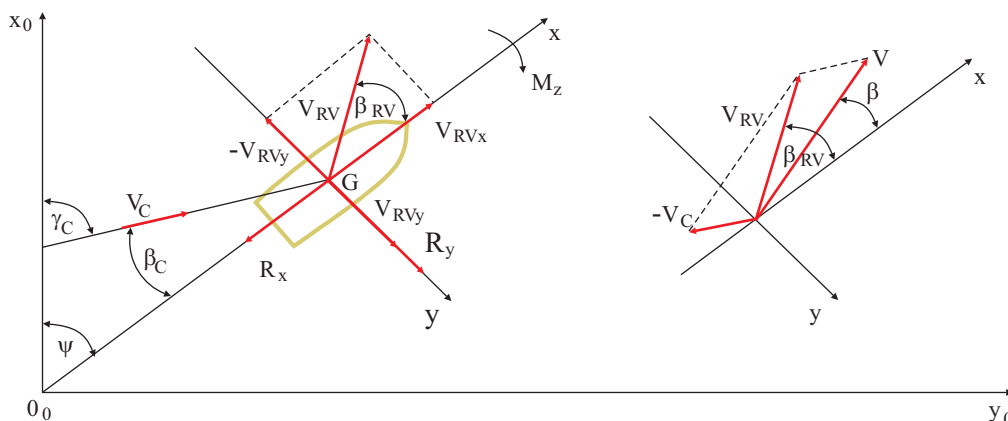


Fig. 3. Relative ship speed and drift angle in still water with surface sea current .

An example of calculated values of the coefficients C_x , C_y , C_m (β_{RV}) acc. [7] is shown in Fig.4. The shown coefficients were determined from the model tests [18] but only for small values of the drift angle β_{RV} (where, as often used, the angles are linearly dependent on the angle β_{RV}).

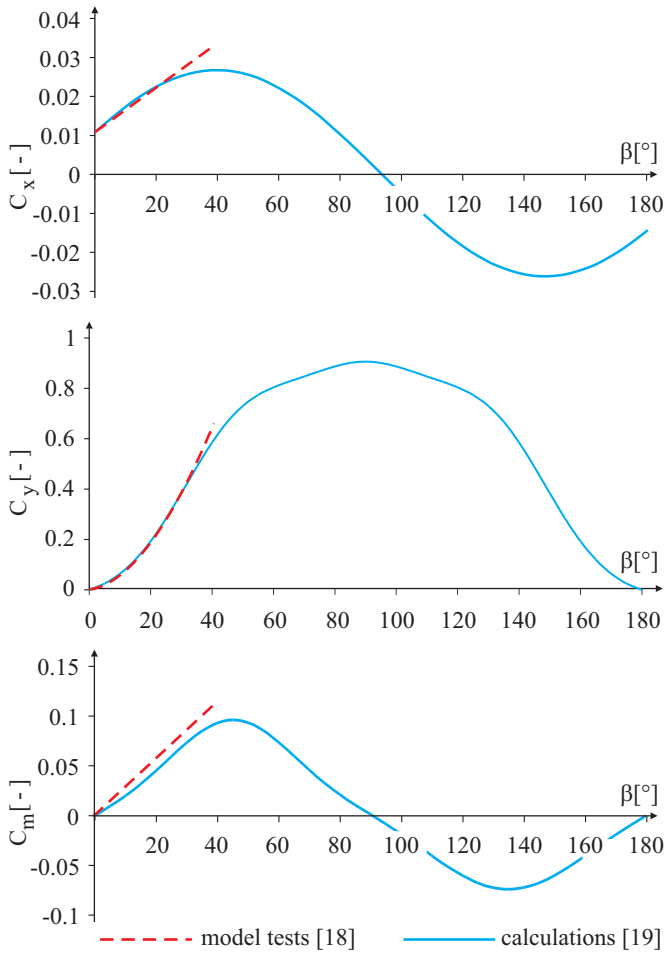


Fig. 4. Ship resistance coefficients for the ship K1* during motion at the speed $V = 8.4$ m/s and a drift angle, as calculated, acc. [20].

Inserting the relations between the drift angle β_{RV} and the ship speed V_{RV} into Eq. (11) one obtains :

$$C_x = 0.075 \sin \left[\left(180^\circ - \arcsin \frac{C_{x_0}}{0.075} \right) \left(1 - \frac{\arccos \frac{V_{RVx}}{V_{RV}}}{k_x} \right) \right]$$

$$C_y = -C_1 \frac{V_{RVx}^2 V_{RVy}}{V_{RV}^3} - C_2 \frac{V_{RVy} |V_{RVy}|}{V_{RV}^2} +$$

$$-16 C_3 \frac{V_{RVx}^4 V_{RVy}^3 |V_{RVy}|}{V_{RV}^8} \quad (12)$$

$$C_m = -2m_1 \frac{V_{RVx} V_{RVy}}{V_{RV}^2} - m_2 \frac{V_{RVy}}{V_{RV}} +$$

$$-8m_3 \frac{V_{RVx}^3 V_{RVy}^3}{V_{RV}^6} - 16m_4 \frac{V_{RVx}^4 V_{RVy}^3 |V_{RVy}|}{V_{RV}^8}$$

* the parameters and dimensions of the ships for which the relevant calculations will be presented in Part III of this paper.

The coefficients C_x , C_y , C_m in the form (12) make it possible to easily calculate the drifting speed V_y and thus the drift angle, provided the components of the external forces exciting ship drift are known.

The coefficient C_{x_0} which appears in the first of Eqs (12), can be calculated from still-water resistance for ship in rectilinear motion and without drift :

$$C_{x_0} = \frac{C_R(V)}{\frac{1}{2} \rho S} \quad (13)$$

where :

$C_R(V)$ – the still-water resistance coefficient for ship in rectilinear motion :

$$C_R(V) = \frac{R}{V^2} \quad (14)$$

and

R – still-water resistance for ship in rectilinear motion.

As the coefficient $C_R(V)$ has no constant value (Fig. 5) hence the resistance R or coefficient C_{x_0} will be provided for a given ship also in the form of the table of discrete values dependent on the speed V . For a given ship its resistance can be approximately measured by means of model testing or derived from approximate formulae e.g. those provided by Holtrop-Mennen method [13, 14, 15] or Hollenbach method [12].

The resistance R to a large extent depends on hull surface state. The above mentioned methods make it possible to take into account a real state of hull surface and thus to investigate its impact on ship's service speed, that has been used in the presented method.

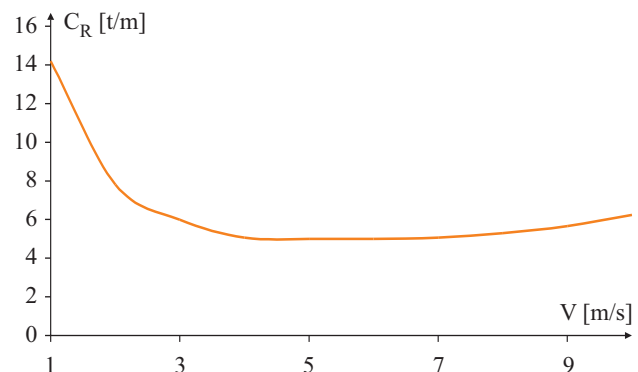
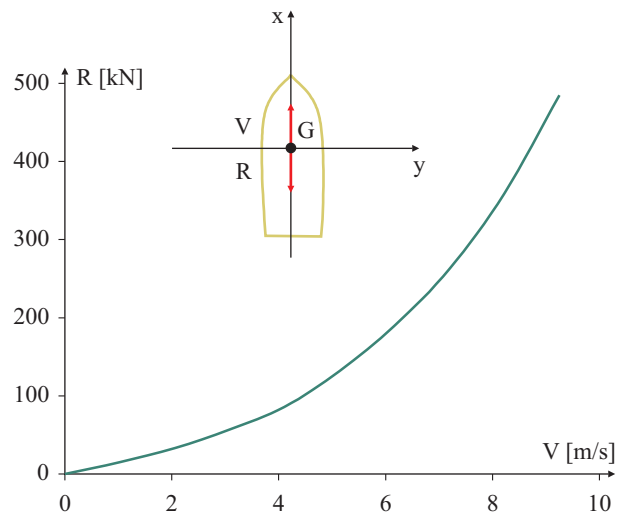


Fig. 5. Example characteristics $R(V)$ and $C_R(V)$ for the ship K1.

WIND INFLUENCE ON SHIP IN MOTION

The mean wind forces acting on the ship in motion can be calculated by using the following formulae :

$$\begin{aligned} R_{xA} &= -\frac{1}{2} \rho_A S_x V_{RA}^2 C_{Ax}(\beta_{RA}) \\ R_{yA} &= \frac{1}{2} \rho_A S_y V_{RA}^2 C_{Ay}(\beta_{RA}) \\ M_{zA} &= \frac{1}{2} \rho_A S_y L V_{RA}^2 C_{Am}(\beta_{RA}) \end{aligned} \quad (15)$$

where :

- ρ_A – air density
- S_x, S_y – areas of front and side projections of above water part of ship onto midship and symmetry plane of ship, respectively
- L – ship length
- V_{RA} – relative wind speed (Fig.6)
- $C_{Ax}, C_{Ay}, C_{Am}(\beta_{RA})$ – aero-dynamical drag coefficients of the above-water part of ship surface, dependent on the relative wind direction (β_{RA})
- β_{RA} – relative wind direction (Fig.6)

$$V_{RA} = \sqrt{V_{RAx}^2 + V_{RAy}^2} \quad (16)$$

$$\left. \begin{aligned} V_{RAx} &= V_A \cos \beta_A - V \\ V_{RAy} &= V_A \sin \beta_A \end{aligned} \right\} \quad (17)$$

$$\beta_A = \gamma_A - \psi + 180^\circ \quad (18)$$

where : β_A – wind direction relative to ship

$$\beta_{RA} = \arctg \frac{-V_{RAy}}{V_{RAx}} \quad (19)$$

- V_A – absolute wind speed
- γ_A – geographical direction of wind ($\gamma_A = 0^\circ$ – north wind, $\gamma_A = 90^\circ$ – east wind)
- V – ship speed
- ψ – geographical course of ship.

In Eqs. (15) the ship drift angle β was omitted because of its small value and very low influence on the relative wind speed β_{RA} and thus on the wind impact forces.

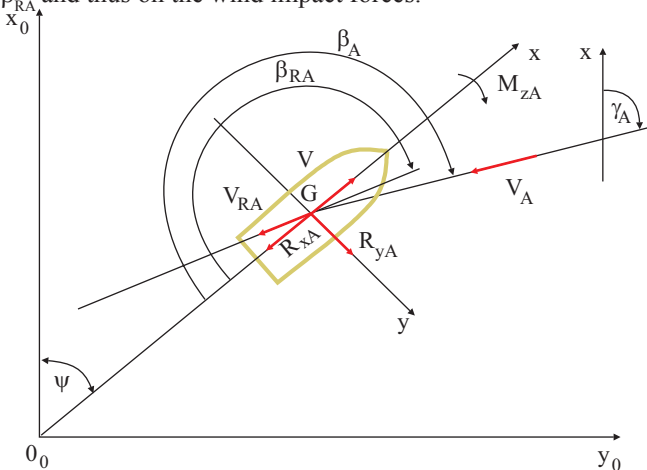


Fig. 6. The reference frames of coordinates, speeds and directions of ship and wind.

One can calculate the wind forces acting on the ship in motion at a given ship speed V and course ψ , assuming the wind parameters (V_A, γ_A), the aero-dynamical drag coefficients C_{Ax}, C_{Ay}, C_{Am} calculated by means of the approximate formulae given in [17, [21] or derived from the model tests [2] for the ship K1 as shown in Fig.7. In Eqs. (15) the force R_{xA} represents the additional resistance due to wind, and the force R_{yA} and moment M_{zA} may induce ship drift and change of its course, and ship's steering gear must be used to balance it, and due to the gear action the additional resistance R_{xR} will be then produced.

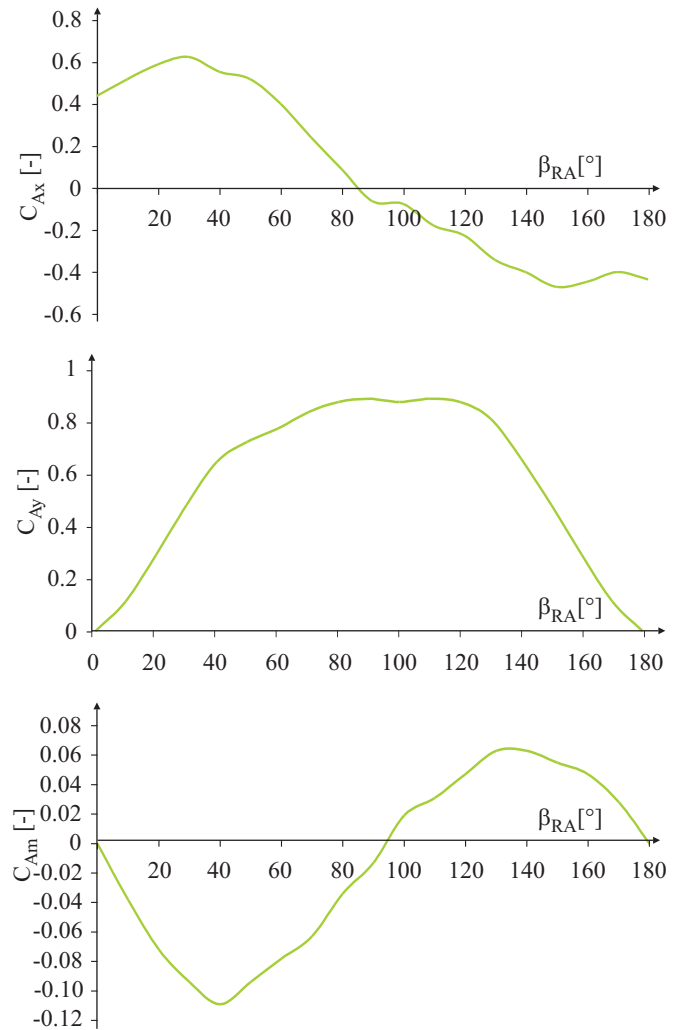


Fig. 7. The aero-dynamical drag coefficients C_{Ax}, C_{Ay}, C_{Am} for the ship K1, acc. [2].

WAVE INFLUENCE ON SHIP IN MOTION

The mean irregular-wave-generated forces (i.e. mean wave-generated drift forces) acting onto ship in motion can be calculated by using the formulae :

$$\left. \begin{aligned} R_{xW} &= 2\rho g \frac{B^2}{L} \int_0^\infty C_{Wx}(\omega/\beta_W, V) S_{\zeta\zeta}(\omega) d\omega \\ R_{yW} &= 2\rho g \frac{B^2}{L} \int_0^\infty C_{Wy}(\omega/\beta_W, V) S_{\zeta\zeta}(\omega) d\omega \\ M_{zW} &= 2\rho g B^2 \int_0^\infty C_{Wm}(\omega/\beta_W, V) S_{\zeta\zeta}(\omega) d\omega \end{aligned} \right\} \quad (20)$$

where :

- ρ – water density
 - g – acceleration of gravity
 - B – ship breadth
 - $C_{w_x}, C_{w_y}, C_{w_m}(\omega / \beta_w, V)$ – coefficients of regular-wave-generated drift force dependent on the wave direction relative to ship, β_w , and ship speed V
 - ω – regular wave frequency
 - β_w – wave direction relative to ship (Fig.8)
- $$\beta_w = \mu - \psi + 180^\circ \quad (21)$$
- μ – geographical direction of waves, ($\mu = 0^\circ$ - north wave, $\mu = 90^\circ$ - east wave)
 - $S_{\xi\xi}(\omega)$ – wave energy spectral density function (dependent on the significant wave height H_s and mean wave period T_1).

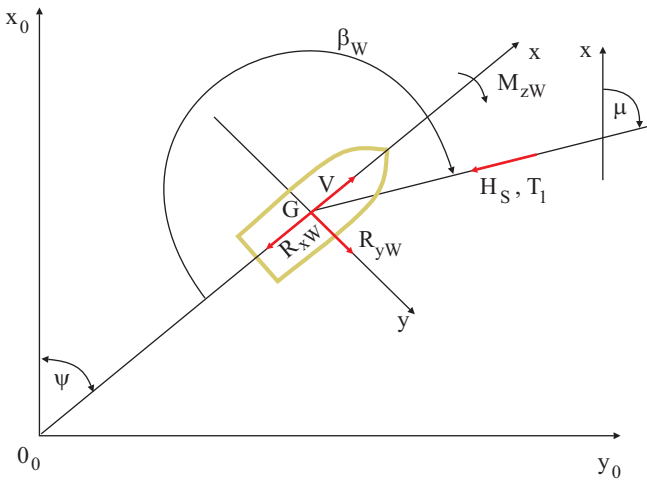


Fig. 8. Mean wave forces acting onto ship.

Assuming the wave parameters (H_s, T_1, μ), and the coefficients of wave – generated drifting force, $C_{w_x}, C_{w_y}, C_{w_m}$, (calculated acc. [1, 5] or derived from the model tests as for the ship K1, shown in Fig.9), one can calculate, for a given ship speed V and course ψ , the wave-generated forces acting on the ship in motion. As in the case of wind action the force R_{xw} represents the additional ship resistance due to wave action, and the force R_{yw} and moment M_{zw} may cause ship drift and change its course.

ADDITIONAL SHIP RESISTANCE DUE TO PASSIVE RUDDER

When ship sails in waves, especially when oblique wind and waves influence the ship's motion, are generated lateral forces and moments which force the ship's course changing

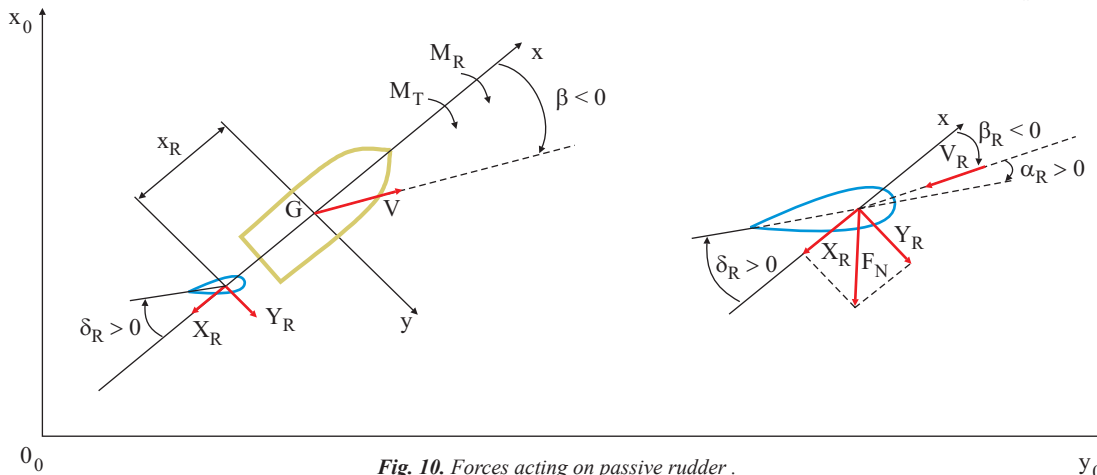


Fig. 10. Forces acting on passive rudder.

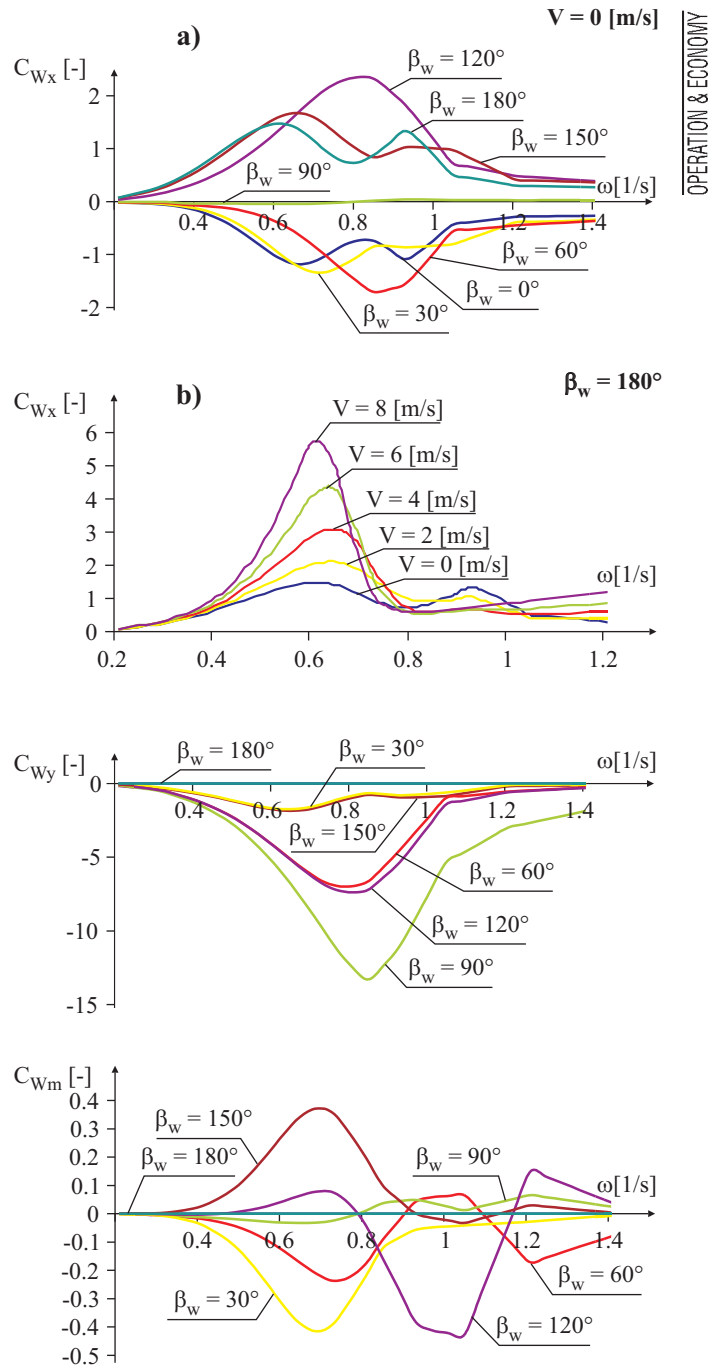


Fig. 9. Wave-generated drift force coefficients $C_{w_x}, C_{w_y}, C_{w_m}$ for the ship K1, acc. [8]:
a) for various wave directions relative to ship at $V = \text{const}$,
b) for various ship speed at $\beta_w = \text{const}$.

and drifting. In order to keep the ship's course constant the rudder blade must be inclined, that produces the additional resistance R_{xR} .

In the literature on ship manoeuvring several algorithms for calculation of hydro-dynamical forces on passive rudder, including those dealing with additional resistance, can be found, e.g. in [9, 16]. According to [16], the passive rudder forces can be calculated by using the formulae:

$$\begin{aligned} R_{xR} &= |F_N \sin \delta_R| \\ R_{yR} &= a_y F_N \cos \delta_R \end{aligned} \quad (22)$$

$$M_{zR} = a_z F_N \cos \delta_R$$

where:

δ_R – passive rudder angle
 a_y – coefficient of hull influence on the rudder force R_{yR}
 a_z – coefficient of hull influence on the rudder moment M_{zR}

$$a_z = a_y X_R \quad (23)$$

X_R – abscissa of rudder axis measured from the ship mass centre G ($X_R < 0$)

F_N – rudder normal force

$$F_N = \frac{1}{2} \rho \frac{6.13 \lambda}{\lambda + 2.25} A_R V_R^2 \sin \alpha_R \quad (24)$$

λ – rudder aspect ratio
 A_R – rudder surface area
 V_R – water inflow velocity to rudder
 α_R – effective rudder angle of attack.

As a result of passive rudder inclination the moment M_{zR} of force R_{yR} appears, and in order to keep the set course of the ship, the rudder moment should have such value as to balance the resultant forcing moment due to action of wind, water flow and waves:

$$M_{zT} = -M_{zR} \quad (25)$$

where:

$$M_{zT} = M_{zA} + M_{zW} + M_z \quad (26)$$

Hence, value of the rudder angle δ_R , calculated by using Eq. (22) under assumption of keeping the ship course constant, will be dependent on the wind and wave parameters and ship's drift angle.

NOMENCLATURE

A_R – rudder surface area
 a_z, a_y – coefficients of hull influence on rudder forces
 B – ship breadth
 C_{Ax}, C_{Ay}, C_{Am} – aero-dynamical drag coefficients
 C_R – still-water ship resistance coefficient
 C_x, C_y, C_m – water resistance coefficients of forces and moments
 C_{wx}, C_{wy}, C_{wm} – coefficients of regular -wave -generated drift force
 C_1, C_2, C_3, C_{x0} – approximation coefficients dependent on form of underwater part of ship hull
 F_N – rudder normal force
 f_{HT} – occurrence probability of wave of H_S and T_1 parameters, coming from μ direction
 f_{VA} – occurrence probability of mean wind speed
 f_{YA} – occurrence probability of wind direction
 f_{μ} – occurrence probability of wave direction
 g – acceleration of gravity

H_S – significant wave height
 k_x – approximation coefficient dependent on form of underwater part of ship hull
 L – ship length
 M_{zT} – resultant forcing moment due to wind, water flow and waves
 m_1, m_2, m_3, m_4 – approximation coefficients dependent on form of underwater part of ship hull
 R – still-water resistance of ship
 R_C – total resistance of ship
 R_x, R_y, M_z – still-water ship resistance components of force and moment during sailing at drift angle β , respectively
 R_{xA}, R_{yA}, M_{zA} – mean wind forces and moment acting on ship in motion (where R_{xA} - additional wave-generated ship resistance), respectively
 R_{xR}, R_{yR}, M_{zR} – passive rudder forces and moment (where R_{xR} - additional rudder-generated resistance), respectively
 R_{xW}, R_{yW}, M_{zW} – mean wave-generated drift forces and moment (where R_{xW} - additional wave-generated resistance), respectively
 S – area of side projection of underwater part of ship hull onto its plane of symmetry
 S_x, S_y – areas of front and side projections of above water part of ship onto midship and symmetry plane of ship, respectively
 S_{ω}^{ω} – wave energy spectral density function
 T – ship draught
 T_1 – mean characteristic wave period
 V – ship speed
 V_A – wind speed
 V_C – sea current speed
 V_R – water inflow velocity to rudder
 V_{RA} – relative wind speed
 V_{RV} – relative ship speed
 V_x, V_y – ship speed components
 X_R – rudder axis abscissa measured from ship mass centre
 α_R – effective rudder angle of attack
 β – ship drift angle
 β_A – wind direction relative to ship
 β_C – current direction relative to ship
 β_{RA} – relative wind direction
 β_{RV} – relative drift angle
 β_W – wave direction relative to ship
 γ_A – geographical direction of wind
 γ_C – geographical direction of sea current
 ΔR – additional resistance due to rough weather
 δ_R – passive rudder angle
 λ – rudder aspect ratio
 μ – geographical direction of wave
 ρ – water density
 ρ_A – air density
 ψ – geographical angle of ship course
 ω – regular wave frequency

BIBLIOGRAPHY

1. Baker M.A.: *Voyage Simulation: A Whole Ship Model Approach*. International Shipbuilding Progress, Vol. 37, No. 411, 1990
2. Blendemann W.: *Manoeuvring Technical Manual*. Schiff und Hafen, Heft 3/1990, Heft 4/1991
3. Bowditch N.: *The American Practical Navigator*. National Imagery And Mapping Agency, 1995
4. Buxton L.L., Raptakis G.: *A Techno-economic approach to the comparison of underwater coatings for new ships*. The Proceedings of the Sixth International Symposium on Practical Design of Ship and Mobile Units. PRADS '95, Sept. 17-22, 1995
5. Chachulski K.: *Fundamentals of ship propulsion* (in Polish). Maritime Publishing House (Wydawnictwo Morskie). Gdańsk 1988

6. Driemljug W.W.: *Nautical oceanography* (in Polish), Maritime Publishing House (Wydawnictwo Morskie). Gdańsk, 1974
7. Dudziak J.: *Algorithm for predicting the seakeeping qualities of a ship-like offshore object floating in waves in conditions of limited water depth and sea current* (in Polish). CTO Report No. RH-88/Z-83. Gdańsk, 1988
8. Dudziak J., Szczuka E., Pawlik A.: *User's manual of WARES software. Short-term prediction of seakeeping qualities of a ship in spatial regular waves* (in Polish). Report No. RH-87/U-001, Ship Hydrodynamics Division of Ship Design and Research Centre (Ośrodek Hydromechaniki Okrętu, Centrum Techniki Okrętowej). Gdańsk, 1990
9. Hirano M.: *On the calculation method of ship manoeuvring motion at the initial design phase*, Journal of the Society of Naval Architects of Japan, Vol. 147. 1980
10. Hogben N., Dacunha N.M.C., Olliver G.F.: *Global Wave Statistics*. BMT. 1986
11. Hogben N., Lumb F.E.: *Ocean Wave Statistics*. National Physical Laboratory. London, 1967
12. Hollenbach K.U.: *Estimating resistance and propulsion for single-screw and twin-screw ship*. Ship Technology Research 45/2. 1998
13. Holtrop J.: *A Statistical Re-analysis of Resistance and Propulsion Data*. International Shipbuilding Progress, No. 363. 1984
14. Holtrop J.: *A Statistical Resistance Prediction Method with a Speed Dependent Form Factor*. Proceedings of the 17th Session BSHC, Varna 17-22 Oct. 1988, Vol. 1.
15. Holtrop J., Mennen G.G.J.: *An Approximate Power Prediction Method*. International Shipbuilding Progress, Vol. 29, No. 335. 1982
16. Inoue S., Hirano M., Kijima K., Takashima J.: *A practical calculation method of ship manoeuvring motion*. International Shipbuilding Progress, Vol. 28, No. 325. 1981
17. Isherwood M.R.: *Wind resistance of merchant ship*. The Royal Institution of Naval Architects, Vol. 115. 1973
18. Kaliciński J., Zdybek T.: *Prediction of hydrodynamical characteristics of underwater parts of Roll on - Roll off ships* (in Polish). 10th Symposium on Ship Hydromechanics. Ship Design and Research Centre (Centrum Techniki Okrętowej). Gdańsk, 1993, Vol. II
19. Szelangiewicz T., Żelazny K.: *Simulation of ship motion in rough sea conditions* (in Polish), Conference on Operational problems of seagoing and inland waterways ships and port facilities, EXSPLO-SHIP'99. Międzyzdroje 09÷13 May 1999, Vol. 2
20. Voitkounski Y.T.: *Ship Theory Handbook*. Sudostroenie. Leningrad, 1985
21. Vorabjew Y.L., Guliev Y.M.: *Application of aerodynamics test results in ships and floating structures at sea problems*, SMSSH '88. The Proceedings of the 17th Session. Varna, Vol. 1, 17÷22 October 1988
22. Wiśniewski B.: *Wind-generated waves* (in Polish), University of Szczecin (Uniwersytet Szczeciński), Dissertations and studies (Rozprawy i studia), Vol. 230. Szczecin, 1998
23. Zdybek T.: *Methods for prediction and assessment of ship seagoing qualities in ship designing* (in Polish), Proceedings of 6th Symposium on Ship Hydromechanics. CTO, Gdańsk 9÷11.X 1985, Vol. 1
24. Zdybek T.: *Prediction and assessment of ship seagoing qualities in ship designing* (in Polish), Shipbuilding and Shipping. (Budownictwo Okrętowe i Gospodarka Morska). Gdańsk, No. 9÷10/1990
25. Żelazny K.: *Numerical prediction of mean long-term service speed of transport ship* (in Polish), Doctorate thesis. Faculty of Maritime Technology, Technical University of Szczecin. 2005

CONTACT WITH THE AUTHORS

Prof. Tadeusz Szelangiewicz
Katarzyna Żelazny, D.Sc., Eng.
Faculty of Marine Technology,
Szczecin University of Technology
Al. Piastów 41
71-065 Szczecin, POLAND
e-mail : tadeusz.szelangiewicz@ps.pl

FOREIGN

conference

SHIP STABILITY WORKSHOP

On 6-7 October 2005 Faculty of Naval Architecture and Ocean Engineering, Istanbul Technical University (ITU) organized :

8th International Ship Stability Workshop

which was initiated by the keynote address on :

Effects of initial bias on the roll response and stability of ships in beam seas
by A.Y. Odabasi and E.Ucer (ITU).

Program of the scientific meeting consisted of 6 topical sessions :

- ◆ ***Theoretical prediction of intact stability*** (4 papers)
- ◆ ***Experimental investigation of intact stability*** (4 papers)
- ◆ ***Special problems on ship stability*** (4 papers)
- ◆ ***Theoretical development in damage stability*** (3 papers)
- ◆ ***Assessment of ship stability safety*** (5 papers) as well as the special session on :

- ▲ Regional issues and activities with one paper on : *Anatomy of a capsized : then and now* – by M. Tyalan (ITU).

The papers presented during the topical sessions were prepared by representatives of the universities and scientific research centers from Japan and USA (4 papers each), Greece and UK (3 papers each), Poland and Russia (2 papers each), Brazil, Holland, Italy, Korea, Norway, Sweden and Turkey (1 paper each).

Polish scientific workers contributed in preparation of the following papers :

- ⊗ ***Appraisal of risk assessment approach to stability of ships*** – by L. Kobylński (Foundation for Safety of Navigation and Marine Environment Protection, Poland)
- ⊗ ***Risk characterization of the requires index R in the New Probabilistic Rules for Damage Stability*** – by M. Pawłowski (Academic Visitor to Ship Stability Research Centre (SSRC); Gdańsk University of Technology, Poland), and D. Vassalos (SSRC; The Universities of Glasgow and Strathclyde, UK).

ASPIS - APPLICATION OF STEEL PANELS INTO SHIP STRUCTURE EUREKA

Project E!3074



This is the name of successive project conducted by Faculty of Ocean Engineering and Ship Technology, Gdańsk University of Technology within the frame of EUREKA European projects



PROJECT DESCRIPTION

Program aim is to introduce into ship structural design a new technology - laser welding techniques. Such techniques make possible to manufacture steel sandwich panels - units which are able to replace some ship hull structural parts like bulkheads, inner bottom structures, flat side surfaces or internal decks, walls etc. It is expected that application of steel sandwich panels will reduce manufacturing costs and also increase internal space. Additionally such 'twinning' of shell plating increase resistance of structure on perforation which rise safety factor in relation to environmentally hazardous cargoes. Although the basic strength characteristics of steel sandwich panels are known as result of previous research programs, implementation such new structure into classical ship hull design requires new knowledge. Project will be focused on complex analysis of simplified structure of typical small and medium size Baltic operated ship in order to replace some parts by sandwich panels. Detail design of new structure especially design of joints will be performed. Numerical calculations and real scale laboratory tests of joints will be carried out to verify applied design approach. Analysis of technical and economical aspects of application of laser welding techniques in ship manufacturing process will be carried out.

The expected result is to create a technically advanced and cost effective new generation of small and medium size Baltic operated ship with implementation of the economically profitable and environmental friendly new technology. Expected results of the project will lead to application of new manufacturing techniques, saving of material and manufacturing costs and reduction of weight of ship structure.

GENERAL AIM

Replacement of shell plating with two-directional system of stiffeners by two shells stiffened by internal unidirectional laser welded stiffeners system.

Expected results of application of the SANDWICH structure :

- ⇒ weight reduction: up to 34 %
- ⇒ costs reduction: about 50 %
- ⇒ increasing of internal space

ACHIEVEMENTS

Design of a technically advanced and cost effective new generation of small and medium size Baltic operated ship structure with implementation of the economically profitable and environmental friendly new technology.

Expected results of the project will lead to application of new manufacturing techniques, saving of material and manufacturing costs and reduction of weight of ship structure. Effect of such approach will give reduction of environment pollutions during manufacturing processes, reduction of manufacturing costs due to new technology implemented as well as reduction of ship operating costs due to better economic indicators.

Area of potential application will be mainly shipbuilding industry but there are some ideas to spread such approach into other market sectors like automotive, railway or civil engineering.

